# High-Energy Astrophysics

Andrii Neronov

November 23, 2016

# Contents

# Chapter 1

# Introduction

The term *"High-Energy Astrophysics"* combines two keywords which determine the scope of the subject.

The "High-Energy" physics conventionally deals with the world of high-energy particles, i.e. particles with energies much higher than the rest energy. For electrons the rest energy is

$$E = m_e c^2 \simeq 5 \times 10^5 \text{ eV} \tag{1.1}$$

(here $m_e = 0.9 \times 10^{-27}$ g is the mass of electron and $c = 3 \times 10^{10}$ cm/s is the speed of light), while for proton it is

$$E = m_p c^2 \simeq 10^9 \text{ eV} \tag{1.2}$$

with the proton mass $m_p = 1.6 \times 10^{-24}$ g. In laboratory conditions here on Earth, the high-energy particles are produced by accelerator machines, like the Large Hadron Collider (LHC) at CERN, in which protons reach energies in the range of 10 TeV. The main goal of the High-Energy Physics research is to understand the fundamental constituents of matter (elementary particles) and interactions between them.
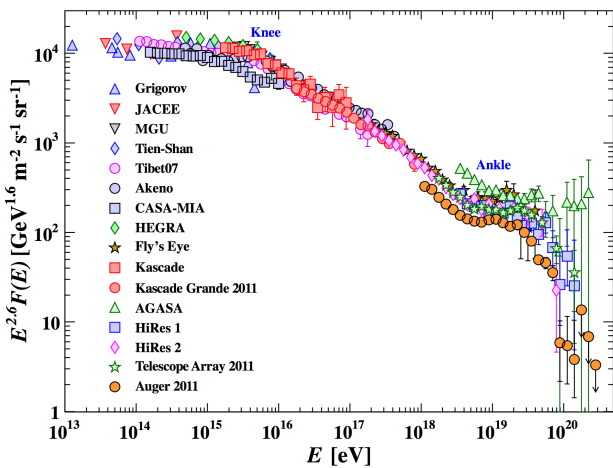


Figure 1.1: The spectrum of cosmic rays measured by different experiments. This log-log scale plot shows the differential flux of particles per unit energy interval, $F(E)$, multiplied by energy $E$ to the power 2.6. From Ref. [4].

Second part of the name High-Energy Astrophysics contains the word *"Astrophysics"* which clearly refers to astronomical observations, typically done using various types of telescopes and aimed at understanding of the properties and mechanisms of activity of different types of astronomical sources, like stars and galaxies.

Combining the two parts into one subject defines the subject of High-Energy Astrophysics as research in the domain of Astronomy, specifically aimed at understanding of the role of high-energy particles and their interactions in the activity of different types of astronomical sources.

The fact that some astronomical objects work as particle accelerators is established based on two types of observational data.

First, we directly detect the high-energy charged particles coming from space in the form of *cosmic rays*. Measurements of the spectrum of cosmic rays (Fig. 1.1) show that the energies of the cosmic ray particles reach $10^{20}$ eV, which is some seven orders of magnitude higher than the maximal energies of protons attained at the LHC.

These particles are produced by some (still unknown) astronomical sources and it is one of the major challenges of modern physics and astronomy to identify these sources. The uncertainty of the sources of cosmic rays constitutes the long-standing *problem of the origin of cosmic rays*. The cosmic rays were first discovered in 1912, so the problem is now 100-year-old.

Next, the information on the presence of high-energy particles in astronomical sources is obtained indirectly, via observations of those sources with telescopes operating at different wavelengths, i.e. with the tools of the *"multi-wavelength astronomy"*. From the early days of the mankind, people have started to do astronomical observations, by looking at the stars on the sky first with the naked eye, and then, starting from Copernicus, with telescopes. Up to the middle of 20th century, the word "astronomical observations" was synonymous to the "astronomical observations in the visible band", because the only type of light sensors used was the human eye, sensitive in the visible range. The visible energy band contains photons in the wavelength range

$$400\text{nm} \leq \lambda \leq 700 \text{ nm} \tag{1.3}$$

This corresponds to a rather narrow range of photon energies $\epsilon = 2\pi\hbar c/\lambda$

$$1.8 \text{ eV} < \epsilon < 3.2 \text{ eV} \tag{1.4}$$

Only astronomical sources emitting photons in this specific energy range were known all this time.

Starting from the end of 1960's, the tools of radio, infrared, ultraviolet, X-ray and gamma-ray astronomy started to develop, so that today, just 50 years after, the energy range available for the astronomical observations comprises some 12 decades in energy:

$$10^{-6} \text{ eV} < \epsilon < 10^{13} \text{ eV} \tag{1.5}$$

Fig. 1.2 shows the definition of different "energy windows" of the multi-wavelength astronomy.
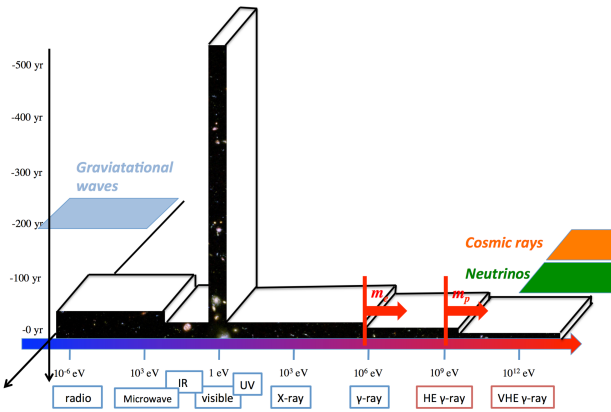


Figure 1.2: Timeline of the history of astronomy and definition of different energy / wavelength bands. and different astronomical "messenger" particles.

The tools of the multi-wavelength astronomy have opened a possibility of observing the effects of interactions of high-energy particles in astronomical sources. Photons with energies up to $10^{13}$ eV are produced by particles with energies at least $E > 10^{13}$ eV, i.e. much higher than the rest energies of proton and electron. These particles emit photons of different energies, from radio to $\gamma$-rays via a variety of emission mechanisms: synchrotorn, Compton scattering, Bremsstrahlung, pion production and decay. Combinaiton of multi-wavelength data is important for getting a complete picture of physical mechanisms of activity of the sources.

In a similar way, the high-energy sources also emit different types of particles, "astronomical messengers". Apart from photons, the most common "astronomical messenger" particles, informaiton on mechanisms of operation of high-energy sources is also carried by neutrinos, cosmic rays and gravitational waves. Combinaiton of the "multi-messenger" data (Fig. 1.2) is equally important for understanding of the mechanisms of operation of sources.

In the context of the multi-wavelength astronomy, the term "High-Energy Astrophysics" is sometimes understood in a slightly different sense, than explained above. the term "High-Energy" might also refer to "photons energies higher than those of the visible / UV light". In this case the "High-Energy Astrophysics" research field comprises all possible sources and physical processes which manifest themselves through the X-ray and gamma-ray emission. This includes then not only processes

related to the presence of relativistic particles in the sources, but also thermal processes in astronomical objects with temperatures in the range above 100 eV (the low-energy boundary of the X-ray band).

## 1.1  Types of astronomical HE sources

Large part of astronomical sources emit radiation with thermal spectrum characterised by temperature $T$. The energies of particles generating this radiation could be estimated from the well-known relation

$$\langle E \rangle \sim \frac{3}{2} k_B T \tag{1.6}$$

where $k_B = 8.6 \times 10^{-5}$ eV K$^{-1}$ is the Boltzmann constant serving as a conversion coefficient between the units of temperature and energy units. Presence of relativistic particles in the thermal astronomical objects implies the temperature range

$$T \sim \frac{m_e c^2}{k_B} \simeq 0.6 \times 10^{10} \text{ K} \tag{1.7}$$

for the objects containing relativistic electrons or

$$T \sim \frac{m_p c^2}{k_B} \simeq 10^{13} \text{ K} \tag{1.8}$$

for the objects with high-energy protons.

The temperature range $T \sim 10^{10}$ K might be reached in the interiors of stars or at the final stage of life of massive stars when they explode as supernovae. The surface temperatures of the stars are typically much lower, not exceeding $10^5$ K, so that solar-like and massive stars powered by the nucleosynthesis reactions are not the sources of interest in the High-Energy Astrophysics domain.

Much higher temperatures are sometimes reached in the objects powered by the release of gravitational (rather than nuclear) energy. A typical first estimate of the temperature of a gravitationally collapsing matter is given by the virial theorem

$$T \sim \frac{2}{3} \frac{\langle E \rangle}{k_B} \sim \frac{1}{3} \frac{U}{k_B} \sim \frac{G_N M m_p}{3 k_B R} \tag{1.9}$$

where $G_N = 6.7 \times 10^{-8}$ cm$^3$/(g s$^2$) is the gravitational constant, $M, R$ are the mass and size of the collapsing matter configuration and $U$ is the gravitational potential energy. Typical particle energies become relativistic, $\langle E \rangle \sim m_p c^2$, if the body is compact enough, with the size

$$R \sim \frac{G_N M}{c^2}. \tag{1.10}$$

This size estimate is about the gravitational radius of a body with the mass $M$

$$R_{grav} = \frac{G_N M}{c^2} \simeq 1.5 \times 10^5 \left[ \frac{M}{M_\odot} \right] \text{ cm.} \tag{1.11}$$

Objects of the size comparable to the gravitational radius are called "compact objects". The known astronomical compact object classes are *neutron stars* and *black holes*, including the supermassive black holes in the centres of galaxies and stellar mass black holes.

These two classes of objects are powering most of the astronomical sources studied in High-Energy Astrophysics, including

- Active Galactic Nuclei (AGN):

- Seyfert galaxies (Sy)

- quasars / blazars (QSO)

- radio galaxies

- X-ray binaries (XRB):

  - Low-mass X-ray binaries (LMXRB)

  - High-mass X-ray binaries (HMXRB)

  - Micorquasars

- end products of the life cycle of massive stars:

  - supernova remnants (SNR)

  - pulsars and pulsar wind nebulae (PWN)

  - gamma-ray bursts (GRB)

Observations using the tools of multi-wavelength astronomy show that significant part of High-Energy Astrophysics sources does not emit radiation with thermal spectrum. Instead, they reveal signal which is spread over many decades of energy. Fig. 1.3 shows an example of such broad band spectrum in the quasar 3C 273. The broad range of photon energies is explained by the broad range of the energies of charged particles (electrons, protons) which have produced the photons. In the particular case of 3C 273, one could see that particle energies should be spread over several decades in energy.

## 1.2 Types of physical processes involved

High-energy particles with broad energy distribution usually loose their energy via various radiative energy loss channels, before being able to "thermalise" (i.e. to establish thermal distribution in momenta). The main radiative (ie. "accompanied by photon production") energy loss channels for electrons are

- synchrotron / curvature radiation,

- inverse Compton emission,

- Bremsstrahlung

A non-radiative energy loss especially important



Figure 1.3: Spectral energy distribution of the quasar 3C 273, in two representations. The upper plot shore the differential flux, which is energy flux per unit energy or frequency. This flux is measured in the units of Jansky, 1 Jy$= 10^{-23}$ erg/(cm$^2$ s Hz). The lower panel show the energy flux as a function of energy. From the Ref. [5].

for mildly relativistic and non-relativistic electrons is
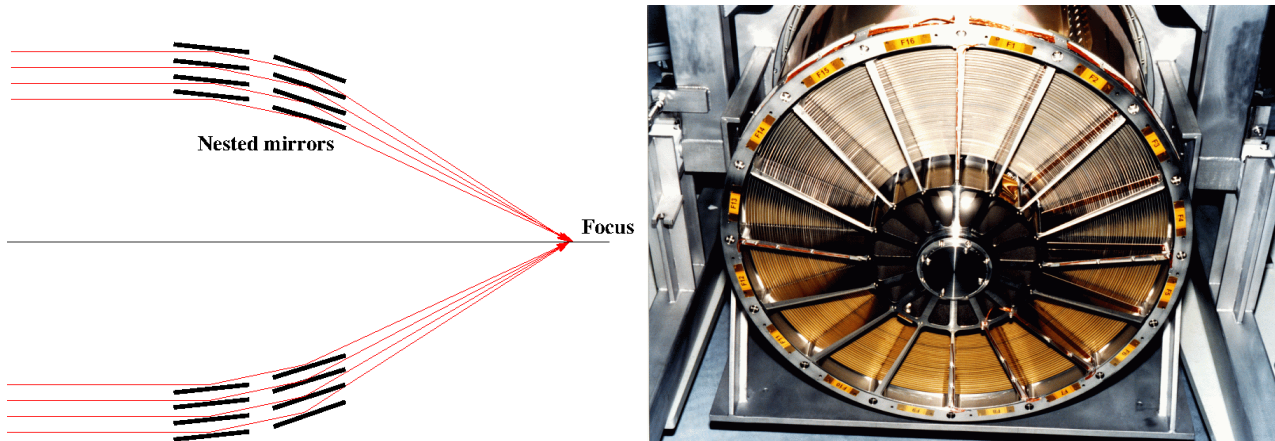
- Coulomb (ionisation) energy loss

Figure 1.4: Left: the principle of grazing incidence optics used in X-ray telescopes. Right: the set of nested mirrors of the X-ray telescope *XMM-Newton*.

All these radiative and non-radiative channels contribute to larger or smaller extent to the formation of spectra of high-energy particles in the sources and to the formation of the broad-band emission spectra of the type shown in Fig. 1.3 for the quasar 3C 273.

In the case of high-energy protons the main radiative energy loss channel is

- production and decay of neutral and charged pions in interactions with matter and radiation fields.

The non-radiative Coulomb losses are also important for the lower energy mildly relativistic protons.

## 1.3 Observational tools

A complete understanding of the physics of sources with photon emission spectra extending from radio to gamma-rays (like 3C 273, shown in Fig. 1.3), is possible only with the detailed information on the imaging, spectral and timing information in all energy bands. This means that the observational tools of High-Energy Astrophysics include telescopes across all energy bands, including radio, infrared, visible, UV, X-ray and gamma-ray bands.

However, the term "experimental / observational High-Energy Astronomy" is usually reserved for telescopes and observational techniques in the X-ray and gamma-ray bands, with the visible / infrared astronomy and radio astronomies considered to be separate disciplines on their own.

X-rays and gamma-rays do not reach the ground. Observations in the X-ray and gamma-ray bands are, therefore, possible only with telescopes placed outside the Earth atmosphere in space. This explains why the age of High-Energy Astronomy has started only at the end of 1960th with the invent of the space flight.

Another peculiarity of the telescopes used in High-Energy Astronomy stems from the fact that, contrary to radio-infrared-visible radiation, X-ray and gamma-ray photons tend to interact with the telescope material in a destructive way, so that it is difficult to focus the signal with the conventional lenses / mirrors without destroying the photons. This is explained by the fact that the energy of each photon is comparable of higher than the ionisation energy of atoms composing the lens / mirror. As a result, the collisions of photons with atoms are inelastic and destructive.

This problem is partially overcome in the X-ray telescopes, where a special type of optical setup enables focusing of X-ray photons with energies up to 10 keV. The principle of the setup, known under the name of "grazing incidence optics", is shown in Fig. 1.4. To avoid the destructive interaction of X-rays with the lens / mirror material, the X-ray photons are falling on the mirror surfaces at large

incidence angles ("grazing" angles). A single grazing incidence focusing mirror (which could be e.g. segments of parabola) would have very small collection area, because it would intercept only a small faction of the X-ray photons. Stacks of nested mirror segments are used to achieve significant collection areas (in the range of $\sim 100 - 1000$ cm$^2$) with the grazing incidence technique. The right panel of Fig. 1.4 shows an example of the mirror of the X-ray telescope XMM-Newton, which is a European Space Agency (ESA) mission now in orbit.
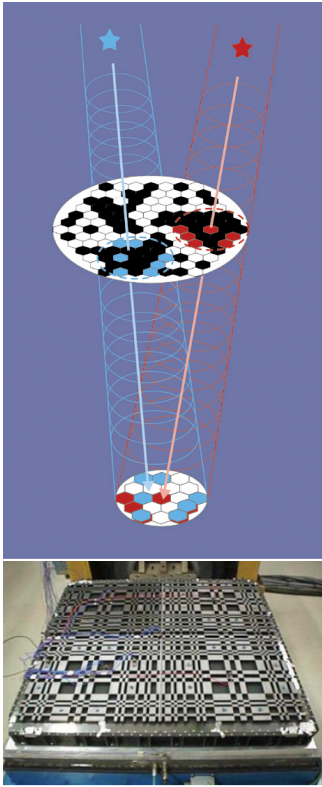


Figure 1.5: The principle of the coded mask optics and the coded mask of IBIS telescope on board of *INTEGRAL*.

Focusing photons of higher and higher energies would require the nested mirror systems with smaller and smaller grazing incidence angles. This, in turn, would imply larger and larger focal lengths. Thus, the grazing incidence technique stops to work at high energies (nowadays about 50 keV, achieved with the NASA X-ray telescope Nu-STAR). At higher energies astronomical observations are done without the use of focusing.

One example of non-focusing optics is the "coded mask" technique, which is a direct development of the method of pinhole camera. This technique is illustrated in Fig. 1.5. Signal from an astronomical source passing through the mask (a plane with a set of holes) casts a particular shadow pattern on the detector plane. Registering this shadow pattern one could determine the source position on the sky via a straightforward ray tracing. Shadow patterns cast by different sources in the field of view overlap, but they are recognisable one-by-one, so that the ray tracing could be done for each source separately. This technique is used in a number of telescope currently operating in the hard X-ray / soft gamma-ray band, including the ESA INTergnational Gamma Ray Laboratory (INTEGRAL). The coded mask of the IBIS imager on board of INTEGRAL is shown in Fig. 1.5.

At the energies higher than $\sim 1$ MeV even the coded mask imaging would not work, because it would require a prohibitively heavy and thick mask which would be able to block gamma-rays. In this energy band telescopes do not use any imaging equipment at all. Instead, each gamma-ray is individually detected and it energy and arrival direction is determined. The observational data consist of the lists of gamma-rays detected from a given region of the sky in a given time span. Positions of sources of gamma-rays on the sky are identified by the clustering of large number of gamma-rays coming from particular directions. This principle of observations is used e.g. by the Fermi gamma-ray telescope operating in the 0.1-100 GeV energy band. Its setup is shown in Fig. 1.6. High-energy gamma-rays entering the telescope are converted into electron-positron pairs in one of the layers of the Tracker (the upper multi-layer part of the detector in Fig. 1.6). Trajectories of electron and positron are "tracked" by the Tracker and then energies of both particles are measured by the Calorimeter, which is the lower thicker layer of the detector shown in Fig. 1.6.

At the energies higher than $\sim 100$ GeV, the space-based detectors are unable to perform sensible astronomical observations, because of their limited collection area. In this energy band, each photon carries macroscopic energy (100 GeV=0.16 erg). The power of astronomical sources is carried by a small number of highly energetic photons and the overall number of photons rapidly decreases with the increase of the energy of each photon. Typical luminosities of astronomical sources are such that in the energy band above 100 GeV only about one or less photons per year could be detected by an instrument with collection area about 1 m$^2$.

Astronomical observations in the Very-High-Energy (VHE) band (photon energies above 100 GeV) are possible only with setups with extremely large collection areas (in the range of $10^4 - 10^6$ m$^2$). Such collection areas are provided by the ground-based Cherenkov telescope arrays, see Fig. 1.7.

The principle of detection of VHE gamma-rays is based on the fact that these gamma-rays produce electromagnetic cascades when they penetrate in the atmosphere. High-energy particles in the cascade move with the speed faster than the speed of light in the air and produce Cherenkov radiation in the UV wavelength range. Large optical reflectors are used to sample this Cherenkov light which appears for short periods of time (about ten nanoseconds) as bright "traces" of the gamma-ray induced cascade in the UV light. The information on the arrival direction and energy of the initial VHE gamma-ray is obtained via stereoscopic imaging of the cascade in the atmosphere (see Fig. 1.7, left panel). Right panel of Fig. 1.7 shows a 17 meter dish of the MAGIC telescope as an example of the large reflectors used by the Cherenkov telescopes.
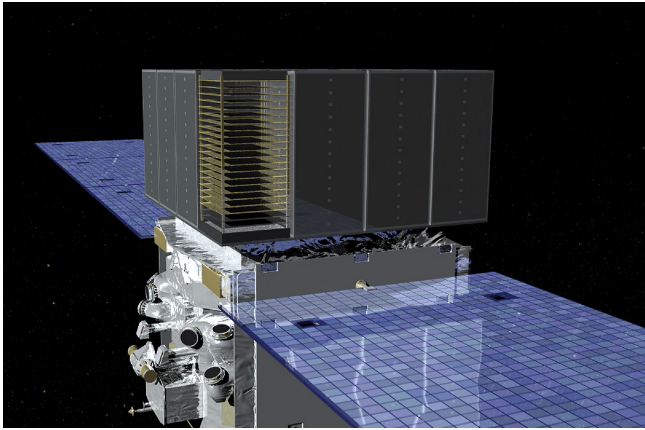
## 1.4 Natural System of Units



Figure 1.6: Fermi LAT telescope. The upper part of the telescope made of many layers is the Tracker. The lower thick layer part is Electromagnetic Calorimeter.

High-Energy Astrophysics subject relates particle physics and astronomy. These two branches of science use different unit conventions and it is sometimes challenging to convert the "language" of particle physicists into the "language" of astronomers and vice versa. A convenient approach is to reduce both astronomical and particle physics quantities and formulae to put them into a common unit system. Throughout this course the common system of units will be the Natural System of Units, with the Gaussian version for electromagnetic quantities (as opposed to Heaviside-Lorentz, with quantities typically differing by $4\pi$ factors between Gaussian and Heaviside-Lorentz systems, see discussion in Ref. [6]).

The idea of the Natural system of units is to reduce the number of fundamental constants to the necessary minimum. This implies typically getting rid of the constants serving for unit conversions. For example, the Boltzman constant $k_B$ serves for conversion between the units of temperature (which is, in essence a measure of energy) and energy:

$$k_B = 8.6 \times 10{-}5 \text{ eV K}^{-1} = 1 \tag{1.12}$$

This means that in the Natural system of units the temperature is always measured in electronvolts, instead of Kelvins. Whenever a measurement is provided in Kelvins, one immediately converts it into electronvolts using the relation

$$1 \text{ K} = 8.6 \times 10^{-5} \text{ eV} \tag{1.13}$$

The same is done with the electric and magnetic permeabilities of vacuum, encountered in the International System of Units:

$$4\pi\epsilon_0 = 4\pi\mu_0 = 1 \tag{1.14}$$

which serve for the introduction of the charge units (Coulomb) in this system.

In a similar way, one could see that the speed of light is, in a sense, a constant for conversion of the units of time and distance: one could measure distance in time units, with the unity the distance travelled by photons in one second, or, vice versa, once could measure time in the distance units, with the unity being time in which photon crosses the distance of 1 cm. Thus, imposing

$$c = 3 \times 10^{10} \text{ cm/s} = 1 \tag{1.15}$$
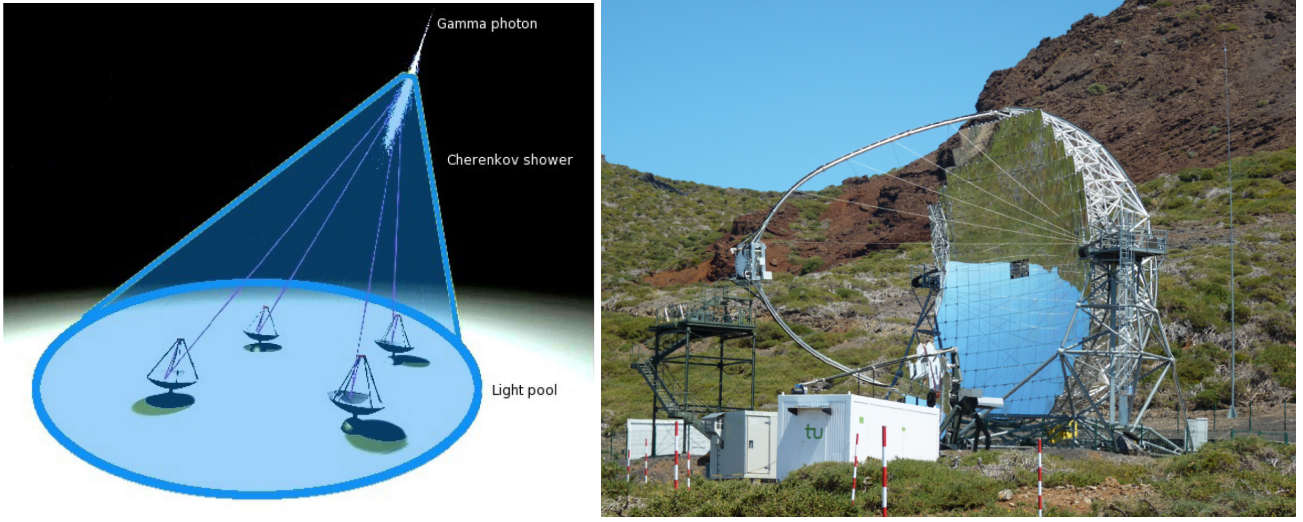
Figure 1.7: Left: the principle of operation of Cherenkov telescopes. RIght: one of the two Cherenkov telescopes of MAGIC stereo pair.

one obtains a conversion between different time-distance units:

$$1 \text{ s} = 3 \times 10^{10} \text{ cm} \tag{1.16}$$

The speed of light serves also for conversion of the units of mass into the units of energy via the relation $E = mc^2$. Thus, any measurement of the mass in grams could be converted into ergs or electronvolts.

The Planck constant relates the energy and frequency of the photon: $E = \hbar\omega$. Setting

$$\hbar = 6.6 \times 10^{-16} \text{ eV s} = 1 \tag{1.17}$$

one obtains a way of measurement of energy in the units of frequency (or inverse time) and vice versa:

$$1 \text{ eV} = 1.5 \times 10^{15} \text{ s}^{-1} \tag{1.18}$$

(notice that the frequency of photons given in the astronomical measurements is usually $\nu = \omega/(2\pi)$, so that the conversion between Hz (frequency of radiation) and eV (energy of photons) differs from the above relation by a $2\pi$ factor.

Combining the conversion of centimetres into seconds and seconds into elevtronvolts one finds a relation

$$\hbar c = 2 \times 10^{-5} \text{ eV cm} = 1, \quad \rightarrow \quad 1 \text{ eV} = 5 \times 10^4 \text{ cm}^{-1} \tag{1.19}$$

In the Natural System of units the electric charge is dimensionless. This is clear from the expression for the fine structure constant:

$$\alpha = \frac{1}{137} = \frac{e^2}{4\pi\epsilon_0 \hbar c} = e^2 \tag{1.20}$$

The numerical value of the electron charge is

$$e = \sqrt{\alpha} \simeq 0.085 \tag{1.21}$$

Magnetic field is measured in the units of $[\text{energy}]^2$, as it is clear from the expression for the energy density of magnetic field

$$U = \frac{\mu_0 B^2}{2} = \frac{B^2}{8\pi} \tag{1.22}$$

The energy density is the quantity measured in e.g. $[\text{eV}/\text{cm}^3]$. Since $cm^{-1}$ is also an energy unit, the units of $U$ are also $[\text{eV}^4]$. To match the dimensions in the right and left hand side of the above equation, $B$ should be measured in the units of $[\text{eV}^2]$. The conversion between Gauss (the units of magnetic field in the CGS system) and $\text{eV}^2$ could be found from the relation

$$U_B = \frac{[B/1\ \text{G}]^2}{8\pi} \frac{\text{erg}}{\text{cm}^3} \tag{1.23}$$

Taking into account the conversion between the energy units ergs and eV

$$1\ \text{eV} = 1.6 \times 10^{-12}\ \text{erg} \tag{1.24}$$

one finds

$$1\ \text{G} \simeq 0.07\ \text{eV}^2 \tag{1.25}$$

The conversion between Tesla (magnetic field units in the International System) and Gauss is

$$1\ \text{T} = 10^4\ \text{G} \tag{1.26}$$

Combining the last and before-last equations one gets a conversion between Tesla and $\text{eV}^2$.

Other useful conversion coefficients which are needed to bring the astronomical and particle physics data to the common system of units are

- energy/power

$$1\ \text{J} = 10^7\ \text{erg} = 6.25 \times 10^{18}\ \text{eV}$$
$$1\ \text{Jy} = 10^{-23}\ \text{erg}/(\text{cm}^2\ \text{s Hz}) \tag{1.27}$$

- distance

$$1\ \text{pc} = 3 \times 10^{18}\ \text{cm}$$
$$1\ \text{AU} = 1.5 \times 10^{13}\ \text{cm}$$
$$1\ \text{Å} = 10^{-8}\ \text{cm} \tag{1.28}$$

- mass / energy

$$1 M_\odot = 2 \times 10^{33}\ \text{g} \simeq 1.8 \times 10^{54}\ \text{erg} \simeq 10^{66}\ \text{eV}$$
$$m_e = 0.9 \times 10^{-27}\ \text{g} = 5 \times 10^5\ \text{eV}$$
$$m_p = 1.7 \times 10^{-24}\ \text{g} = 0.94 \times 10^9\ \text{eV} \tag{1.29}$$

- cross section

$$1\ \text{barn} = 10^{-24}\ \text{cm}^2 \tag{1.30}$$

This set of conversion formulae will be systematically used in numerous numerical estimates encountered in the following chapters.

The dimensionality of magnetic field suggests an important scale of the magnetic field strength, which is

$$B = \frac{m_e^2}{e} \simeq 4 \times 10^{13}\ \text{G} \tag{1.31}$$

This is the field when the giroradius of electrons moving in the magnetic field becomes comparable to their Compton (or de Broglie in the non-relativistic case) wavelength. If magnetic field is higher than

this fundamental level, motions of electrons in magnetic field could not be considered as a classical mechanics problem.

One important note concerns the gravitational force and Newton constant. From the expression of the Newton's law

$$ma = \frac{G_N M m}{r^2} \tag{1.32}$$

it is clear that the dimensionality of the Newton constant is $[\text{mass}]^{-2}$ or, equivalently, $[\text{length}]^2$. This means that it is not possible to set this constant to one in the Natural System of units. Instead, the numerical value of the Newton constant is

$$G_N = 6.7 \times 10^{-8} \frac{\text{cm}^3}{\text{g s}^2} = \frac{1}{(10^{19} \text{ GeV})^2} = \frac{1}{M_{Pl}^2} \tag{1.33}$$

The energy (or mass) scale entering the Newoton's constant is called the Planck scale, it is the scale at which the Compton wavelength of a particle becomes comparable to its gravitational radius.

# Chapter 2

# Radiative Processes

## 2.1 Radiation from a moving charge

Most of the formulae in this chapter for the radiative processes involving electrons (synchrotron and curvature radiation, Compton scattering and Bremmstrahlung emission) are different applications of the basic formulae for the dipole radiation of an accelerated charge. Taking this into account, this section reminds the derivation of the accelerated charge radiation.

Electromagnetic field is a solution of Maxwell equations [7]

$$\frac{\partial F^{\mu\nu}}{\partial x^\nu} = -4\pi j^\mu. \tag{2.1}$$

where $x^\mu = (t, \vec{x})$ are the four-coordinates and $j^\mu$ is the four-current. Expressing the electromagnetic field tensor through the 4-potential $F_{\mu\nu} = \partial_\mu A_\nu - \partial_\nu A_\mu$, we rewrite the Maxwell equations for the potential in the Lorentz gauge $\partial A^\mu / \partial x^\mu = 0$ in the form of inhomogeneous wave equation

$$\frac{\partial^2 A^\mu}{\partial x_\nu \partial x^\nu} = 4\pi j^\mu \tag{2.2}$$

We are interested in the particular case of a point charge $e$ moving along a trajectory $\vec{r} = \vec{r}_0(t)$. Such a charge creates the 4-current $j^\mu = e(\delta(\vec{r} - \vec{r}_0(t)), \vec{v}\delta(\vec{r} - \vec{r}_0(t)))$ where $\vec{v} = d\vec{r}_0/dt$ is the velocity. Solution of the wave equation in a point $\vec{r}$ at the moment of time $t$ is determined by the state of motion of the charge at the moment of time $t'$ implicitly found from the relation

$$t' + \left|\vec{r} - \vec{r}_0(t')\right| = t \tag{2.3}$$

The solution of the system of wave equations for the potential is known to be the Lienard-Wichert potential $A_\mu = (\phi, \vec{A})$

$$\phi(r, t) = \left.\frac{e}{(R - \vec{v} \cdot \vec{R})}\right|_{t'}, \quad \vec{A}(r, t) = \left.\frac{e\vec{v}}{(R - \vec{v} \cdot \vec{R})}\right|_{t'}, \tag{2.4}$$

where $\vec{R} = \vec{r} - \vec{r}_0$. Electric and magnetic fields corresponding to this potential could be calculated from relations $\vec{E} = \partial\vec{A}/\partial t - \partial\phi/\partial\vec{x}$, $\vec{B} = (\partial/\partial\vec{x}) \times \vec{A}$. This gives an expression

$$
\begin{aligned}
\vec{E} &= \frac{e(1 - v^2)}{(R - \vec{v} \cdot \vec{R})^3}(\vec{R} - R\vec{v}) + \frac{e}{(R - \vec{v} \cdot \vec{R})^3}\left[\vec{R} \times \left[(\vec{R} - R\vec{v}) \times \frac{d\vec{v}}{dt}\right]\right] \\
\vec{B} &= \frac{1}{R}\left[\vec{R} \times \vec{E}\right]
\end{aligned}
\tag{2.5}
$$

If the velocity of the charge does not change in time, $dv/dt = 0$, the second term is absent and the first term just gives the Coulomb field of the charge, falling as $R^{-2}$ at large distances. Using the rules of Lorentz transformation of electromagnetic tensor, one finds that in this case the magnetic field is absent in the reference system comoving with the charge.

Accelerated motion of the charge $dv/dt \neq 0$ leads to the appearance of an additional term which falls as $1/R$ at large distances. Both electric and magnetic field due to this term are orthogonal to the direction toward the charge. This is the field of electromagnetic wave generated by the accelerated motion. A qualitative understanding of the appearance of electromagnetic wave could be obtained via a simple geometrical calculation, see e.g. [2, 1].

At large distances from the source, $r \gg r_0$, one could approximate $R \simeq r$. In this case the second term in the expression from the electric field of slowly moving charge could be rewritten in the form

$$\vec{E} \simeq \frac{1}{r} \left[ \left[ \ddot{\vec{d}} \times \vec{n} \right] \times \vec{n} \right] \tag{2.6}$$

where the dipole moment $\vec{d} = e\vec{r}_0$ and the unit vector $\vec{n} = (\vec{r})/r$ are introduced. The magnetic field in these notations is

$$B \simeq \frac{1}{r} \left[ \ddot{\vec{d}} \times \vec{n} \right] \tag{2.7}$$

Both electric and magnetic fields are orthogonal to the direction from the charge to the observation point $\vec{n}$ and they are also orthogonal to each other. Such configuration is typical for the electromagnetic wave propagating in the direction $\vec{n}$. The energy flux carried by the wave is given by the Poynting vector

$$\vec{S} = \frac{\left[ \vec{E} \times \vec{B} \right]}{4\pi} = \frac{B^2}{4\pi} \vec{n} \tag{2.8}$$

Substituting the expression for $B$ one finds the flux $dI$ in the solid angle $d\Omega$ in the direction $n$ at an angle $\theta$ with respect to the direction of $\ddot{\vec{d}}$

$$\frac{dI}{d\Omega} = (\vec{S} \cdot \vec{n}) = \frac{\ddot{d}^2}{4\pi} \sin^2 \theta \tag{2.9}$$

One could see that the intensity of emission is directed in a broad angular range preferentially in the direction orthogonal to the acceleration $\ddot{\vec{d}}$.

Integration of the above expression over $0 < \theta < \pi$ gives ($d\Omega = 2\pi \sin \theta d\theta$)

$$I = \frac{2\ddot{d}^2}{3}. \tag{2.10}$$

This is the Larmor formula for the intensity of dipole radiation by an accelerated charge.

This total power is emitted in the form of photons of different energies. To know the energy distribution, or spectrum, of the radiation we decompose the overall power onto power at a given frequency $\omega$ by doing the Fouriver transform. For this we use the formula of Fourier analysis stating that $\int_{-\infty}^{\infty} |f(t)|^2 dt = 4\pi \int_{-\infty}^{\infty} |f(\omega)|^2 d\omega$. This means that in the non-relativistic motion case

$$\int_{-\infty}^{\infty} \frac{dI}{d\Omega} dt = \int_{-\infty}^{\infty} \frac{|\ddot{d}|^2}{4\pi} \sin^2 \theta dt = \int_{-\infty}^{\infty} \omega^4 |\hat{d}(\omega)|^2 \sin^2 \theta d\omega = \int_{-\infty}^{\infty} \frac{d\hat{I}(\omega)}{d\Omega} d\omega \tag{2.11}$$

and the spectral energy density of radiation at the frequency $\omega$ is

$$\frac{d\hat{I}(\omega)}{d\Omega} = \omega^4 |\hat{d}(\omega)|^2 \sin^2 \theta \tag{2.12}$$

Here the hat denotes the Fourier transform of the function, e.g.

$$d(t) = \int_{-\infty}^{\infty} e^{-i\omega t} \hat{d}(\omega) d\omega \tag{2.13}$$

For a relativistic charge, one introduces the 4-velocity $u^\mu = dx^\mu/d\tau$ where $\tau$ is the proper time along the particle trajectory, and the 4-acceleration $a^\mu = du^\mu/d\tau = (d\gamma/d\tau, d(\gamma\vec{v})/d\tau)$, with $\gamma = 1/\sqrt{1-v^2}$ being the particle gamma factor. The Larmor formula rewritten in the 4-vector notations reads

$$I = \frac{2e^2}{3} a_\mu a^\mu = \frac{2}{3} e^2 \left( \left(\frac{d\gamma}{d\tau}\right)^2 - \left(\frac{d(\gamma\vec{v})}{d\tau}\right)^2 \right) \tag{2.14}$$

Expressing the derivative of $\gamma$ through the derivative of $v$ and substituting $dt/d\tau = \gamma$ one could rewrite the last formula in the form

$$I = \frac{2}{3} e^2 \gamma^6 \left( -(\vec{v}\cdot\dot{\vec{v}})^2 - \frac{1}{\gamma^2}(\dot{\vec{v}})^2 \right) \tag{2.15}$$

where dot denotes the coordinate time derivative $d/dt$. The quantity $(\vec{v}\cdot\dot{\vec{v}}) = va_{\parallel}$ is the component of particle acceleration parallel to the velocity. One could introduce also the normal component of the acceleration via relation $\dot{\vec{v}}^2 = a_{\parallel}^2 + a_{\perp}^2$, so that the Larmor formula becomes

$$I = \frac{2}{3} e^2 \gamma^6 \left( -a_{\parallel}^2 - \frac{1}{\gamma^2} a_{\perp}^2 \right) \tag{2.16}$$

## 2.2 Curvature radiation

Let us consider a relativistic particle with gamma factor $\gamma$ moving along a circle of the radius $R$ with the speed $v$. The angular frequency of such motion is $\omega_0 = v/R$. The only component of acceleration different from zero is $a_{\perp} = \omega_0 v$. The Larmor formula (2.16) gives the total power of emission

$$I = \frac{2}{3} e^2 \gamma^4 \omega_0 v^2 = \frac{2}{3} \frac{e^2 \gamma^4 v^4}{R^2} \tag{2.17}$$

Note that for an ultra-relativistic particle it is always the normal component of acceleration which provides the main contribution to the dipole radiation intensity. This is because $v \simeq 1 - \epsilon$, where $\epsilon \simeq 1/(2\gamma^2) \ll 1$. The rate of change of the of the absolute value of $v$ is always small. Indeed, if the characteristic time scale of the change of particle gamma factor is $\omega_0^{-1}$, one could estimate the value of the parallel component of acceleration as $a_{\parallel} \sim \dot{\gamma}/(\gamma^3) \sim \omega_0/\gamma^2$. Substituting this expression into Eq. (2.16), one finds that the emission power is $I \sim e^2\gamma^2\omega_0^2$, which scales just as a second, rather than forth, power of $\gamma$.

The spectrum of emission from a non-relativistic particle in a circular orbit could be found in a straightforward way. The velocity and acceleration are varying periodically with the period $T = 2\pi/\omega_0$, so that the only non-zero component of the Fourier transform of $d(t)$ is $\hat{d}(\omega_0)$. This means that the emission spectrum (for the non-relativistic motion case) is sharply peaked at the frequency $\omega_0$.



Figure 2.1: Angular pattern of dipole emission from non relativistic (left) and relativistic (right) particles.

The second time derivative of the dipole moment is a vector rotating in the plane of the circular motion of the particle. The angular distribution of the emitted dipole radiation is given by Eq. (2.9) and is shown in the left panel of Fig. 2.1.
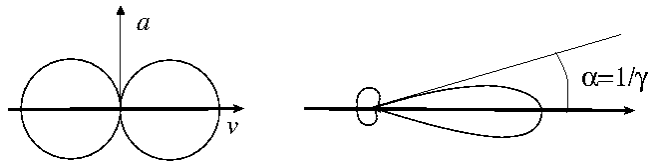
In the relativistic case, the angular distribution pattern changes due to the Doppler boosting. To find the characteristic boosting pattern, consider a particle moving along axis $x$ with the speed $v$ close to the speed of light, $v \sim 1$. In the reference system comoving with the particle, particle motion is non-relativistic and emission (e.g. dipole radiation described above) is in a broad range of angles. The transformation to the comoving reference frame has the form

$$x' = \gamma(x - vt); \quad y' = y, \quad z' = z, \quad t' = \gamma(t - vx). \tag{2.18}$$

Transformation of velocities between the laboratory and comoving frame is

$$u_x = \frac{u'_x + v}{1 - vu'_x}, \quad u_y = \frac{u'_y}{\gamma(1 + vu'_x)}, \quad u_z = \frac{u'_z}{\gamma(1 + vu'_x)}. \tag{2.19}$$

Consider a photon which is emitted in the direction normal to the particle motion along $y$ axis in the comoving frame, $u'_x = u'_z = 0$. In the laboratory frame the components of photon velocity are

$$u_x = v, \quad u_y = \frac{u'_y}{\gamma}, \quad u_z = 0 \tag{2.20}$$

The angle between the direction of motion of photon and particle velocity in the laboratory frame is, therefore,

$$\alpha = \frac{u_y}{u_x} = \frac{1}{v\gamma} \simeq \frac{1}{\gamma} \tag{2.21}$$
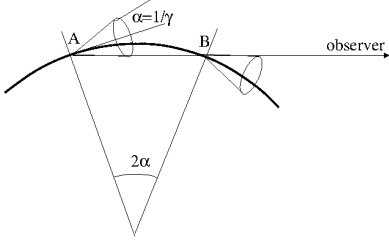


Figure 2.2: Geometry of emission by relativistic particle in circular motion.

A similar estimate, $\alpha \sim \gamma^{-1}$ could be found for the broad range of photon directions in the comoving frame, which are not almost aligned with the direction of particle velocity. Thus, the effect of the Doppler boosting on any broad angle radiation pattern is to compress this pattern into a narrow range of directions $\alpha \lesssim \gamma^{-1}$ around the direction of particle velocity $v$.

Relativistic beaming also dramatically changes the spectrum of radiation. Consider an observer situated in the plane of circular motion at large distance from the particle. (S)he detects the radiation in the form of short pulses, each time when the beam with an opening angle $\alpha \simeq \gamma^{-1}$ directed along particle velocity passes through the line of sight. The duration of the pulse could be readily calculated from geometry shown in Fig. 2.2. The radiation is visible from a fraction of the circle of particle trajectory spanning an angle $2\alpha$. The length of the arc of the angular size $2\alpha$ is $L = 2\alpha R$ and the time interval during which particle emits in the direction of observer is therefore $\Delta t = 2\alpha R/v$. Suppose that the particle passes the point A at the moment $t_0$. The photon emitted at this point arrives at the location of observer after a time delay $\delta t_A = d/c$, where $d$ is the distance to the observer. The last photon in the direction of the observer is emitted at the point B, at the moment $t_A = t_0 + \Delta t$. It arrives at the location of the observer at the moment $t_B = t_0 + \Delta t + \delta t_B$, where $\delta t_B = (d - L)/c$. The overall duration of the pulse seen by the observer is

$$\Delta t_{obs} = t_B - t_A = \Delta t + \delta t_B - \delta t_A = \Delta t \, (1 - v) = \frac{2R}{\gamma v}(1 - v) = \frac{2R}{\gamma^3 v(1 + v)} \simeq \frac{R}{\gamma^3} \tag{2.22}$$

where we have substituted $v \simeq 1$ in the last equality. The Fourier transform of the time sequence of pulses detected by the observer has all harmonics up to the frequency

$$\omega_{curv} \sim \frac{1}{\Delta t_{obs}} \sim \frac{\gamma^3}{R} \tag{2.23}$$

It is useful to have a numeric reference value for this frequency for the future estimates:

$$\epsilon_{curv} = \hbar\omega_{curv} = \frac{\hbar c\gamma^3}{R} \simeq 2 \times 10^4 \left[\frac{\gamma}{10^5}\right]^3 \left[\frac{R}{10^6 \text{ cm}}\right]^{-1} \text{ eV} \tag{2.24}$$

One could understand the above formula in the following way. Relativistic electrons with energies $E_e = \gamma m_e \simeq 100$ GeV confined within a region of the size $R \sim 10$ km, they inevitably emit curvature radiation in the hard X-ray band, at the energies about $\epsilon_{curv} \sim 20$ keV. As an "everyday life" example of such situation one could mention the past times when the LHC accelerator machine in CERN was still electron-positron collider LEP (Large Electron Positron). It was operating at the energies $E \sim 100$ GeV accelerated in the LHC tunnel of the radius $R \sim 10$ km. From Eq. (2.24) one could find that the electron beam was a source of hard X-rays.

Situation when high-energy particles are confined within an astronomical source of finite size is typical. Thus, generically, all astronomical sources hosting high-energy particle accelerators should be visible in telescopes, because the charged high-energy particles confined within the source emit (at least!) curvature radiation photons.

Particles emitting curvature radiation loose energy at the rate

$$\frac{dE_e}{dt} = -I \simeq \frac{2}{3}\frac{e^2\gamma^4}{R^2} \simeq 4 \times 10^{11} \left[\frac{\gamma}{10^5}\right]^4 \left[\frac{R}{10^6 \text{ cm}}\right]^{-2} \frac{\text{eV}}{\text{s}} \tag{2.25}$$

(see Eq. (2.17)). Once injected in such a compact region of space, TeV electrons loose all their energy within the time interval shorter than one second. Coming back to the LEP example, one could conclude from Eq. (2.25) that supporting the beam of accelerated electrons in the LEP accelerator machine required continuous "re-acceleration" of the beam. All the beam energy was continuously dissipated into the hard X-rays.

## 2.2.1 Astrophysical examples (pulsar and black hole magnetospheres)

The reference example illustrating curvature radiation in astrophysical environments is the currently most often considered model of $\gamma$-ray emission from magnetospheres of pulsars.

Pulsars are strongly magnetised and fast spinning neutron stars, i.e. compact stars of the size $R_{NS} \sim 10^6$ cm, rotating at frequencies $1 - 10^3$ Hz and possessing magnetic fields in the range of $B \sim 10^{12}$ G. Most of the isolated point sources of GeV $\gamma$-rays in the Galactic Plane are pulsars. Spectrum of emission from the brightest pulsar on the sky, the Vela pulsar, is shown in Fig. 2.3.

The bright GeV $\gamma$-ray emission from the pulsars is pulsed at the period of rotation of the neutron stars $(1 - 10^3$ Hz). This implies that the $\gamma$-ray photons are produced close to the neutron star, in a region reasonably close to the surface of the neutron star. We adopt a first estimate $R \sim R_{NS} \sim 10^6$ cm and leave further details for the dedicated section on pulsars. This emission is detected at the energies exceeding 1 GeV. It is inevitably produced by relativistic particles.



Figure 2.3: Spectrum of pulsed $\gamma$-ray emission from Vela pulsar (the brightest GeV $\gamma$-ray point source on the sky). From Ref. [8].

As it is mentioned above, relativistic particles confined to a compact spatial region inevitably loose energy at least onto curvature radiation (there might be competing energy loss channels, we will consider them later on). Using Eq. (2.24) one could estimate the energies of electrons responsible
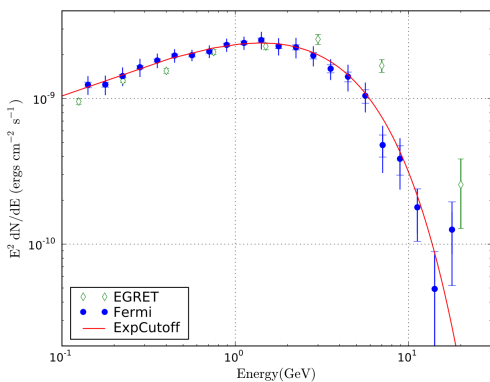
for the observed $\gamma$-ray emission, under the assumption that the $\gamma$-rays are produced via curvature mechanism

$$E_e \simeq 2 \times 10^{12} \left[ \frac{\epsilon_{curv}}{1 \text{ GeV}} \right]^{1/3} \left[ \frac{R}{R_{NS}} \right]^{1/3} \text{ eV} \qquad (2.26)$$

Assumption that emission observed in pulsars comes from the curvature radiation process provides, in a sense an upper bound on the energies of particles contained in the sources. Indeed, we will see later on in the course that most of the radiation processes encountered in High-Energy Astrophysics are different variations of one and the same process of dipole radiation. Each time when trajectories of relativistic particles are deflected by some force, they start to radiate. The slowest possible deflection rate and, respectively, the largest possible extent of particle trajectory is when particle is deviated only when it crosses the entire astronomical source where it is confined. The slowest possible deflection rate leads to the "minimal" energy loss rate and to the emission of lowest energy photons. This is the case of curvature radiation with $R$ $R_{NS}$ in pulsars. From these arguments one could conclude that typical energies of electrons confined around pulsars are

$$E_{e, \, pulsars} \lesssim 10^{12} \text{ eV} \qquad (2.27)$$

This conclusion just stems from an observational fact that most of the pulsars have high-energy cut-offs in the spectra in the GeV energy band. It does not depend on the details of the model of particle acceleration and interactions which lead to the observed $\gamma$-ray emission.

A similar argument is applicable to any astronomical source. As another example, we can take an Active Galactic Nucleus (AGN) powered by a supermassive black hole of the mass $M$ and, respectively, of the size $R_g \gtrsim G_N M \simeq 10^{14} \left[ M/10^9 M_\odot \right]$ cm. In such sources, $\gamma$-rays with energies up to 10 TeV are detected (see Fig. 2.4 for an example of a nearby AGN M87). Assuming (without much justification based on model building) that the 10 TeV photons are produced via curvature radiation mechanism, $\epsilon_{curv} \sim 10$ TeV, we could use a re-scaled equation 2.26 to find an upper bound on the typical energy of electrons confined close to the black hole:



Figure 2.4: Spectrum of $\gamma$-ray emission from vicinity of supermassive black hole in M87 galaxy, from Ref. [9].

$$E_{e, \, AGN} \lesssim 2 \times 10^{16} \left[ \frac{\epsilon_{curv}}{10 \text{ TeV}} \right]^{1/3} \left[ \frac{R}{10^{14} \text{ cm}} \right]^{1/3} \text{ eV} \quad (2.28)$$

Note that the energy loss via curvature radiation occurs for any charged relativistic particle confined in a finite region. For example, protons with the same gamma factor as electrrons and, respectively, the energy which is $m_p/m_e = 2 \times 10^3$ times higher than electrons, produce the same curvature radiation. Thus, along with a conclusion that the AGN central engine, the supermassive black hole, does not contain electrons with energies in excess of $2 \times 10^{16}$ eV, we could also conclude that it does not contain protons with energies much in excess of

$$E_{p, \, AGN} \lesssim 4 \times 10^{19} \left[ \frac{\epsilon_{curv}}{10 \text{ TeV}} \right]^{1/3} \left[ \frac{R}{10^{14} \text{ cm}} \right]^{1/3} \text{ eV} \qquad (2.29)$$

Curvature radiation also provides the "minimal possible" energy loss for high-energy particles confined in an astronomical source (e.g. a pulsar or a supermassive black hole in the AGN). In the
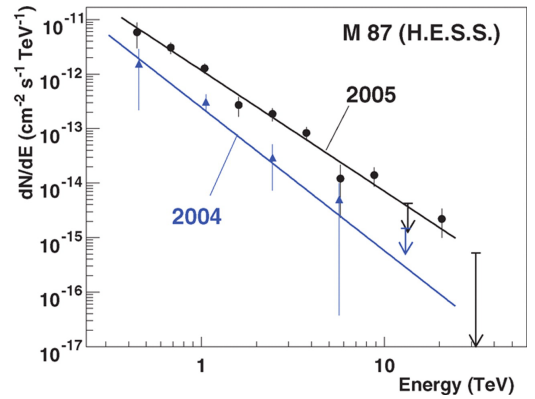
absence of competing more fast energy losses, a high-energy particle living in the source would loose most of its energy onto electromagnetic emission on a time scale

$$
\begin{aligned}
t_{curv} &= \frac{E_e}{dE_e/dt} = \frac{3m_e^4 R^2}{2e^2 E_e^3} \simeq 2 \times 10^{-5} \left[\frac{E_e}{1 \text{ TeV}}\right]^{-3} \left[\frac{R}{10^6 \text{ cm}}\right]^2 \text{ s} \\
&\simeq 0.2 \left[\frac{E_e}{10^{16} \text{ eV}}\right]^{-3} \left[\frac{R}{10^{14} \text{ cm}}\right]^2 \text{ s}
\end{aligned}
\tag{2.30}
$$

which could be estimated from the rate of energy loss by electrons (2.25). In both the pulsar and AGN example, this time scale is, in fact, comparable or shorter than the time in which particles moving with the speed of light cross the region of the size about the size of the source,

$$
t_{lc} = \frac{R}{c} \simeq 3 \times 10^{-5} \left[\frac{R}{10^6 \text{ cm}}\right] \text{ s} \simeq 3 \times 10^3 \left[\frac{R}{10^{14} \text{ cm}}\right] \text{ s}
\tag{2.31}
$$

Thus, in both examples, high-energy particles have to be continuously "regenerated" inside the source on a very short time scale, by an efficient acceleration process.

## 2.3 Evolution of particle distribution with account of radiative energy loss

A competition between acceleration, energy loss and escape processes leads to formation of broad energy distribution of high-energy particles inside astronomical sources

$$
\frac{dN_e}{dE} = f_e(E).
\tag{2.32}
$$

The index $e$ is introduced to distinguish the distribution of charged high-energy particles, e.g. electrons, from the distribution of photons emitted by these particles, which we will denote as $dN_\gamma/dE$.

The acceleration process injects particles of energy $E$ with a rate $Q_e(E)$. Then particles are cooling due to radiative and non-radiative losses, with a rate $\dot{E}$, which is also a function of energy. As a result, their energy decreases and $f_e(E)$ at the injection energy decreases, while $f_e(E - \int \dot{E}dt)$ increases. Particles do not disappear once injected, so that the function $f_e(E)$ should satisfy a continuity equation in the energy space

$$
\frac{\partial f_e}{\partial t} + \frac{\partial}{\partial E}\left(\dot{E}f_e(E)\right) = Q_e(E,t)
\tag{2.33}
$$

The sense of this equation is that the increase / decrease of $f_e$ in a unit time in a given energy bin of the width $\Delta E$ at reference energy $E$ is given by the rate of injection $Q_e \Delta E$, by the rate influx of particles from the adjacent higher energy bin, $-\dot{E}f(E)\Big|_{E+\Delta E}$ and the rate of outflow into the adjacent lower energy bin $-\dot{E}f(E)\Big|_{E}$ ($\dot{E} < 0$ is "velocity" along the energy axis, compare with the continuity equation of the fluid dynamics: $\partial f/\partial t + \vec{\nabla}(f\vec{v}) = Q$ ).

In the above equation, $Q$ is a source of particles, but could also be the "leakage" of particles (then it is negative). The leakage, or escape of particles is often characterised by typical escape time $\tau_{esc}$, which could be a function of energy. Then, the source / leakage term, from dimensional reasons, has the form

$$
Q_{e,esc} = \frac{f_e}{\tau_{esc}(E)}
\tag{2.34}
$$

so that the Eq. (2.33)

$$
\frac{\partial f_e}{\partial t} + \frac{\partial}{\partial E}\left(\dot{E}f_e(E)\right) = Q_e(E,t) - \frac{f_e}{\tau_{esc}}
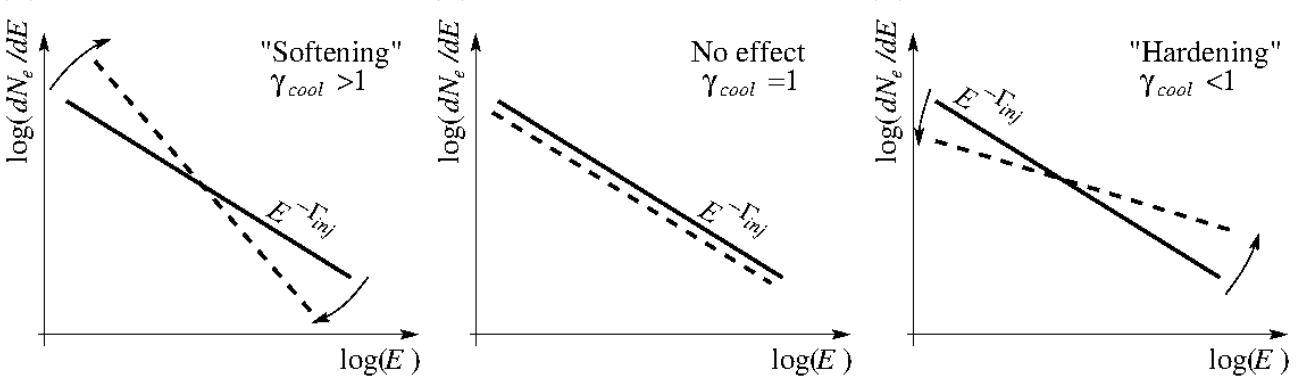\tag{2.35}
$$

Figure 2.5: The effect of cooling on particle spectrum for different energy dependance of the cooling rate.

In the steady state situation, $\partial f/\partial t = 0$, in the absence of escape $\tau_{esc} \to \infty$, the solution of the above equation has the form

$$f_e(E) = \frac{1}{\dot{E}} \int_E^\infty dE' \, Q_e(E') \tag{2.36}$$

As an example, let us calculate the energy distribution of particles reached in the situation where the injection is a delta-function in energy $Q(E) \sim \delta(E - E_0)$. In this case the above solution of the equation takes the form

$$f_e(E) = \begin{cases} 1/\dot{E}, & E < E_0 \\ 0, & E > E_0 \end{cases} \tag{2.37}$$

If the cooling is provided by the curvature radiation, then $\dot{E} \sim E^4$ and

$$f_e(E) = \begin{cases} AE^{-4}, & E < E_0 \\ 0, & E > E_0 \end{cases} \tag{2.38}$$

where $A$ is a normalisation factor. One could see that cooling leads to a "pile up" of particles at lower energies: the number of particles per unit energy interval (or per decade in energy) increases with the decrease of their energy.

Another useful example is when both the injection and the cooling are powerlaw type functions: $Q_e(E) \sim E^{-\Gamma_{inj}}$, $\dot{E} \sim E^{\gamma_{cool}}$ ($\gamma_{cool} = 4$ in the case of curvature radiation). Taking the integral in Eq. (2.36) we find

$$f_e(E) = AE^{1-\Gamma_{inj}-\gamma_{cool}} \tag{2.39}$$

The resulting spectrum is also a powerlaw in this case. Thus, if $\gamma_{cool} > 1$, cooling of particles due to an energy loss leads to a "pile up" of particles at low energies. In the case when $\gamma_{cool} = 1$ (we will see later on that this is the case e.g. for the Bremsstrahlung cooling mechanism), cooling does not change the initial injection spectrum. If $\gamma_{cool} < 1$ (this is the case for e.g. the non-radiative ionisation loss), cooling makes the particle spectrum harder, because the low energy particles are "washed out" by the faster cooling, than the higher-energy particles. Different effects of "cooling" on the particle spectrum are illustrated in Fig. 2.5.

## 2.4  Spectrum of emission from a broad-band distribution of particles

One could see from the previous subsection that typically high-energy particles are distributed over a wide energy range (e.g. form a powerlaw type spectra), rather than concentrate around a particular

energy. Broad distribution of energies of emitting particles leads to a broad distribution of energies of emitted photons.

In general, the spectrum of emission from a distribution of electrons (protons) $dN_e/dE = f_e(E_e) \sim E_e^{-\Gamma_e}$ could be calculated once the spectrum of emission from mono energetic electrons $\Phi(E_e, E_\gamma)$ is known. The intensity $\Phi$ of emission at the energy $E_\gamma$ depends on the electron energy $E_e$. The emission from the distribution of electrons is given by the integral

$$\phi(E_\gamma) = \int \frac{dN_e}{dE_e} \Phi(E_e, E_\gamma) dE_e \qquad (2.40)$$

Let us calculate the spectrum of curvature emission from a powerlaw distribution of electrons $dN_e/dE = f_e(E_e) \sim E_e^{-\Gamma_e}$ in the particular case of curvature radiation. Electrons of the energy $E_e$ emit curvature photons of the energy given by Eq. (2.24), $E_{\gamma,*} \sim E_e^3$. In the first approximation one could adopt a "delta-function approximation" for the spectrum of emitted photons, $\Phi(E_e, E_\gamma) \sim \delta(E_\gamma - E_{\gamma,*})$. The normalisation of the emission spectrum is proportional to the rate of emission of photons , given by Eq. (2.25), the emission power, divided by the photon energy $E_\gamma = E_e^3/(m_e^3 R)$.

$$\Phi(E_e, E_\gamma) = \frac{E_e}{m_e R} \delta\left(E_\gamma - \frac{E_e^3}{m_e^3 R}\right) \qquad (2.41)$$

Substituting this expression into (2.40) and taking the integral, we find

$$\begin{aligned}
\phi(E_\gamma) & \sim \int E_e^{-\Gamma_e} \frac{E_e}{m_e R} \delta\left(E_\gamma - \frac{E_e^3}{m_e^3 R}\right) dE_e \\
& \sim \int \frac{E_e^{1-\Gamma_e}}{m_e R} \frac{m_e^3 R}{3 E_e^2} \delta\left(E_\gamma - \frac{E_e^3}{m_e^3 R}\right) d\left(\frac{E_e^3}{m_e^3 R}\right) \\
& \sim E_e^{-\Gamma_e - 1} \sim E_\gamma^{\frac{-\Gamma_e - 1}{3}}
\end{aligned} \qquad (2.42)$$

Thus, the spectrum of emission from a power law distribution of emitting particles is also a power law.

We can generalise the above formula for an arbitrary dependence of the power of emission on the electron energy, $P(E_e) \sim E_e^{\gamma_{cool}}$ ($\gamma_{cool} = 4$ in the case of curvature radiation) and an arbitrary relation between photon and electron energy, $E_{\gamma,*} \sim E_e^\sigma$, ($\sigma = 3$ in the case of curvature emission). This gives

$$\phi(E_\gamma) \sim E_\gamma^{\frac{\gamma_{cool} + 1 - \Gamma_e - 2\sigma}{\sigma}} \qquad (2.43)$$

We will reuse this formula to calculate the spectra of synchrotron, Compton and Bremsstrahlung emission in the following paragraphs.

In a particular case when the shape of the particle spectrum is affected by the effects of cooling (see Eq. 2.39),

$$\Gamma_e = \Gamma_{inj} + \gamma_{cool} - 1 \qquad (2.44)$$

the emission spectrum is independent on the energy scaling of the cooling rate $\gamma_{cool}$:

$$\phi(E_\gamma) \sim E_\gamma^{\frac{2 - 2\sigma - \Gamma_{inj}}{\sigma}} \qquad (2.45)$$

Examples of powerlaw (or cut-off powerlaw) spectra of emission from a distribution of high-energy particles could be found in Figs. 2.3, 2.4. Publicaitons in X-ray and $\gamma$-ray astronomy often give representation of the spectrum in the form

$$\frac{dN_\gamma}{dE}(E_\gamma) \sim \phi(E_\gamma), \text{ "differential spectrum" or}$$

$$E_\gamma \frac{dN_\gamma}{dE}(E_\gamma) \sim E_\gamma \phi(E_\gamma), \text{ "photon spectrum" or}$$

$$E_\gamma^2 \frac{dN_\gamma}{dE}(E_\gamma) \sim E_\gamma^2 \phi(E_\gamma), \text{ "spectral energy distribution"} \qquad (2.46)$$

| Cooling law: | | $\dot{E} \propto E_e^{\gamma_{cool}}$ |
|---|---|---|
| Relation between photon and electron energies: | | $E_\gamma \propto E_e^\sigma$ |
| Electron spectrum: | | $dN_e/dE_e \propto E_e^{-\Gamma}$ |
| Emission spectrum: | | $dN_\gamma/dE_\gamma \propto E_\gamma^{\frac{\gamma_{cool}+1-\Gamma_e-2\sigma}{\sigma}}$ |
| Evolution of electron spectrum: | | $\Gamma_{inj} \to \Gamma_{inj} + \gamma_{cool} - 1$ |
| | $\gamma_{cool}$ | $\sigma$ |
| curvature radiation | 4 | 3 |
| synchrotron radiation | 2 | 2 |
| inverse Compton (T) | 2 | 2 |
| inverse Compton (KN) | 0 | 1 |
| Bremsstrahlung | 1 | 1 |

The first representation for the photon flux, in units of "photons/(cm$^2$s eV)" is called the "differential spectrum", i.e. it is the photon count rate per unit detector area per unit time and *per unit energy interval.* The second representation provides a fair judgement of the signal statistics in different energy bands, because it gives the count rate of photons per unit detector area *per decade of energy.* Finally, the third representation, often called "Spectral Energy Distribution" or SED of the source, provides an estimate of the " emitted power per energy decade". This representation is useful for building physical models of the sources. It allows to judge in which energy band most of the source power is emitted.

## 2.5   Cyclotron emission / absorption

Considering the curvature radiation, we have assumed that the emitting charged particle moves along a circular trajectory of an arbitrary radius $R$. In the particular example of pulsars, this radius was estimated to be comparable to the size of the emitting system (about 10 km, which is the size of the neutron star). Another possibility is that the emitting particles are confined to much smaller distance scales than the entire source size.

This is the case for the particles moving in magnetic fields. In this case particles spiral along magnetic field lines, being confined within the distance equal to the gyroradius $R_L$. The gyroradius is readily found from the second law of Newton,

$$ma = \frac{mv^2}{R_L} = evB \tag{2.47}$$

which gives

$$R_L = \frac{mv}{eB} \tag{2.48}$$

The angular frequency of gyration is just

$$\omega_B = \frac{v}{R_L} = \frac{eB}{m} \simeq 12 \left[ \frac{B}{10^{12} \text{ G}} \right] \left[ \frac{m}{m_e} \right]^{-1} \text{ keV} \tag{2.49}$$

Non-relativistic particles moving in magnetic field emit dipole radiation at the frequency (energy) $\omega_B$. This emission is called cyclotron emission. This emission is difficult to observe (remember that astronomical observations start from radio band, in the frequency range starting from 100 MHz, which correspond to photons of the energies higher than $10^{-6}$ eV. If the magnetic field in an object is lower than $\sim 100$ G, the cyclotron emission is not observable. At the same time, strong magnetic fields in astronomical sources might reveal themselves through the characteristic cyclotron emission features.

## 2.5.1   Astrophysical example (accreting pulsars)

Such features are observed in the spectra of X-ray accreting pulsars. These systems contain magnetised neutron stars, but there is no particle acceleration in the pulsar magnetosphere. Instead, there is ionised matter right next to the surface of the neutron star. The neutron star is magnetised, so that electrons and protons/nuclei gyrate in the magnetic field. The magnetic field is the dipole field of the star, so it is very homogeneous (on small distance scales).

The gyroradius of electrons in the strong dipole field of the neutron star is extremely small:

$$R_L = \frac{m_e v}{eB} \simeq 10^{-9} v \left[\frac{B}{10^{12}\ \mathrm{G}}\right]^{-1}\ \mathrm{cm} \qquad (2.50)$$

This is a microscopic radius which is comparable to the deBroglie wavelength

$$\lambda_{dB} = \frac{1}{m_e v} \simeq 4 \times 10^{-11} v^{-1}\mathrm{cm} \qquad (2.51)$$

If

$$B > \frac{m_e^2 v^2}{e} \simeq 4 \times 10^{13} v^2\ \mathrm{G} \qquad (2.52)$$

the spread of electron wavefunction is larger than the gyroradius. This means that the motion of electrons in magnetic field should be considered as a quantum mechanical problem.

In the quantum mechanical settings, we are solving the Schroedinger equation

$$\hat{H}\Psi = E\Psi \qquad (2.53)$$

with the Hamiltonian

$$\hat{H} = \frac{1}{2m}\left(\hat{\vec{p}} - e\vec{A}\right)^2 \qquad (2.54)$$

For magnetic field directed along $z$ axis, $B_z \neq 0$, the vector potential $\vec{A}$ could be chosen in the form

$$A_y = xB; A_x = A_z = 0. \quad \vec{B} = \vec{\nabla} \times \vec{A} = (0,0,B). \quad (2.55)$$

The resulting Schroedinger equation is then

$$\frac{1}{2m}\left[-\left(\frac{\partial}{\partial x}\right)^2 + \left(i\frac{\partial}{\partial y} - exB\right)^2 - \left(\frac{\partial}{\partial z}\right)^2\right]\Psi = E\Psi \qquad (2.56)$$

The Hamiltonian does not depend on $y, z$, so that $p_y, p_z$ is are integrals of motion. The $i\partial/\partial z\ i\partial/\partial y$ in the above equation could then be replaced by $p_y, p_z$ eigenvalues:

$$\frac{1}{2m}\left[-\left(\frac{\partial}{\partial x}\right)^2 + (p_y - exB)^2\right]\Psi = \left(E + \frac{p_z^2}{2m}\right)\Psi \quad (2.57)$$
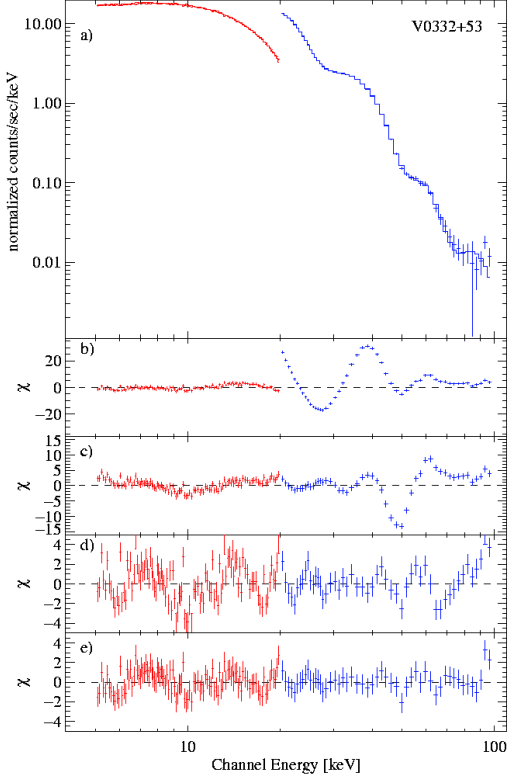


Figure 2.6: Spectrum of X-ray accreting pulsar V 0332+53, showing a series of cyclotron lines [10]. Upper panel shows the overall spectrum, lower panels show the deviations of the data from the model, first without inclusion of the lines, and then after addition of one, two three cyclotron lines. The spectrum is in "normalised counts" units, which is just a histogram of photon counts in a given energy bin. It is different from the conventional spectra in physical units of flux (e.g. "photons per cm$^2$ and second"). Conversion from "normalised counts" to physical units requires a knowledge of energy response of the detector.

The last equation is a Schroedinger equation with quadratic potential, i.e. is that of a harmonic oscillator. The solutions of this equation are known to form a discrete spectrum

$$E_n - \frac{p_z^2}{2m} = (n + 1/2)\frac{eB}{m} = (n + 1/2)\omega_B \tag{2.58}$$

Thus, electrons moving in strong magnetic field close to the neutron star sit on discrete energy levels (called Landau levels), similarly to electrons in an atom.

Similarly to electrons in atoms, the spectra of emission and absorption from electrons at Landau levels are discrete. Being the spectra of harmonic oscillators, they are formed by series of equidistant lines. Measurement of the line energies provides a measurement of the magnetic field close to the neutron star surface. Fig. 2.6 shows an example of observation of cyclotron line series in the spectrum of one of the accreting pulsars, V 0332+53, done by INTEGRAL telescope [10].

The line energies are in the 10 keV band. From Eq. (2.49) we infer that the magnetic field strength in the photon emission region is about $10^{12}$ G. This magnetic field is much stronger than the fields which are encountered in laboratory conditions (which are $\lesssim 10^5$ G for the strongest man-made magnets). They are also much higher than the fields of normal stars. The magnetic fields at the surface of the Sun reach at most kG strengths.

## 2.6   Synchrotron emission

Cyclotron emission / absorption is produced by non-relativistic particles gyrating in magnetic field. If the particles are relativistic, the properties of the dipole electromagnetic radiation due to the gyration in magnetic field change.

Basic relations for the energy of synchrotron photons and power of synchrotron emission could be found directly from the formulae for dipole and, in particular, for curvature radiation simply via substitution of the relativistic expression for the gyroradius (the relativistic analog of Eq. (2.48))

$$R_L = \frac{E_e}{eB} \simeq 3 \times 10^7 \left[\frac{E_e}{10^{10} \text{ eV}}\right] \left[\frac{B}{1 \text{ G}}\right]^{-1} \text{ cm} \tag{2.59}$$

instead of an arbitrary $R$ in the corresponding formulae. This exercise with Eq. (2.24) gives

$$\epsilon_{synch} = \frac{\gamma^3}{R_L} = \frac{eBE_e^2}{m_e^3} \simeq 5 \left[\frac{B}{1 \text{ G}}\right] \left[\frac{E_e}{10^{10} \text{ eV}}\right]^2 \text{ eV} \tag{2.60}$$

for the energy of synchrotron photons. Note that contrary to the energy of curvature radiation photons, which scales as $E_e^3$, the energy of the synchrotron photons grows only as $E_e^2$ with the increase of the electron energy. This is because the curvature radius of electron trajectory expands with increasing electron energy.

Substituting $R_L$ at the place of $R$ in Eq. (2.25) we find the energy loss rate on the synchrotron emission:

$$-\frac{dE_e}{dt} \simeq \frac{2}{3}\frac{e^4 B^2 E_e^2}{m_e^4} \simeq 4 \times 10^5 \left[\frac{B}{1 \text{ G}}\right]^2 \left[\frac{E_e}{10^{10} \text{ eV}}\right]^2 \text{ eV/s} \tag{2.61}$$

The energy loss rate grows only as $E_e^2$ with the increase of the electron energy. The synchrotron loss time is then

$$t_{synch} = \frac{E_e}{-dE_e/dt} = \frac{3m_e^4}{2e^4 B^2 E_e} \simeq 2 \times 10^4 \left[\frac{B}{1 \text{ G}}\right]^{-2} \left[\frac{E_e}{10^{10} \text{ eV}}\right]^{-1} \text{ s} \tag{2.62}$$

We could also re-use the results of Section 2.4 to find the spectrum of a broad band distribution of electrons, e.g. from a powerlaw type spectrum with the slope $\Gamma_e$:

$$\frac{dN_e}{dE_e} \sim E_e^{-\Gamma_e} \tag{2.63}$$

Repeating the calculation leading to Eq. 2.43 we find that for the synchrotron emission both parameters $\gamma_{cool}$ and $\sigma$ are equal to 2, so that the spectrum of synchrotron emission has the photon index

$$\phi(E_\gamma) = \frac{dN_\gamma}{dE_\gamma} \sim E_\gamma^{-\Gamma_{synch}}, \quad \Gamma_{synch} = \frac{\Gamma_e + 1}{2} \tag{2.64}$$

We could also re-use the formulae for the evolution and steady state spectra of particles with account of energy loss, derived in Section 2.3, to understand the influence of the synchrotron energy loss on the spectrum of high-energy electrons. The evolution of the spectrum of electrons is governed by Eq. (2.35) with the energy loss rate being due to the synchrotron emission, Eq. (2.61). In the absence of escape, its general steady state solution has the form (2.36).

In the particular case of mono energetic injection, $Q(E) \sim \delta(E - E_0)$, the solution has the form (2.37), which in the case of $\dot{E} \sim E^2$ is

$$\frac{dN_e}{dE_e} \sim \begin{cases} E_e^{-2}, & E < E_0 \\ 0, & E > E_0 \end{cases} \tag{2.65}$$

More generally, if the acceleration process results in injection of electrons in the energy range above some limiting lowest energy (the injection spectrum has a low-energy cut-off), synchrotron cooling leads to formation of an $E^{-2}$ type spectrum of the "cooling tail" below the minimal injection energy.

The synchrotron emission from the "cooling tail" has a powerlaw-type spectrum with the slope $\Gamma_{synch} = (2+1)/2 = 1.5$, see Eq. (2.64).

Another useful example if that of the effect of synchrotron energy loss on the powerlaw type injection spectrum $Q(E) \sim E^{-\Gamma_{inj}}$. In this case, substituting $q_{cool} = 2$ into Eq. (2.39) we find

$$\frac{dN_e}{dE_e} \sim E_e^{-(\Gamma_{inj}+1)} \tag{2.66}$$

Thus, synchrotron cooling leads to a "softening" of the initial injection spectrum $\Gamma_{inj} \to \Gamma_{inj}+1$. This corresponds to a larger and larger "pile up" of the cooled electrons at lower and lower energies. Such a "pile up" could be understood qualitatively if one recalls that the kinetic equation (2.35) describes motion of particles in energy space. The speed of this motion, $\dot{E}$ is decreasing with the decrease of the energy, so that the particles get gradually "stuck" while movingg to lower energy bins. This leads to accumulation of larger number of particles in lower energy bins.

Suppose that the injection spectrum is an $E^{-2}$ type powerlaw (this is typical slope of the spectrum resulting from the shock acceleration, as we will see later on). Synchrotron cooling would soften the spectrum down to an $E^{-3}$ type spectrum. The photon index of the synchrotron emission from the cooled distribution of electrons would then have the slope $\Gamma = (3+1)/2 = 2$.

## 2.6.1 Astrophysical example (Crab Nebula)

A prototypical example of the high-energy source is Crab nebula, which is a nebular emission around a young ($10^3$ yr old) pulsar. It is one of the brightest $\gamma$-ray sources on the sky and serves as a calibration target for most of the $\gamma$-ray telescopes. The spectrum of emission from the Crab nebula spans twenty decades in energy, from radio (photon energies $10^{-6}$ eV) up to the Very-High-Energy $\gamma$-ray (photon energies up to 100 TeV) band. Large, parsec-scale size and moderate distance (2 kpc) to the nebula enable detailed imaging of the source in a range of energy bands, from radio to X-ray. The composite radio-to-X-ray image of the nebula is shown in Fig. 2.7, top panel.

Radio to X-ray and up to GeV $\gamma$-ray emission from the nebula presents a composition of several broad powerlaw-type continuum spectra, with the photon indices changing from $\Gamma \simeq 1.3$ in the radio-to-far-infrared band to $\Gamma \simeq 2.2$ in the 1-100 MeV band. Such powerlaw type spectra extending down to the infrared and radio domains are commonly interpreted as being produced by the synchrotron emission mechanism.
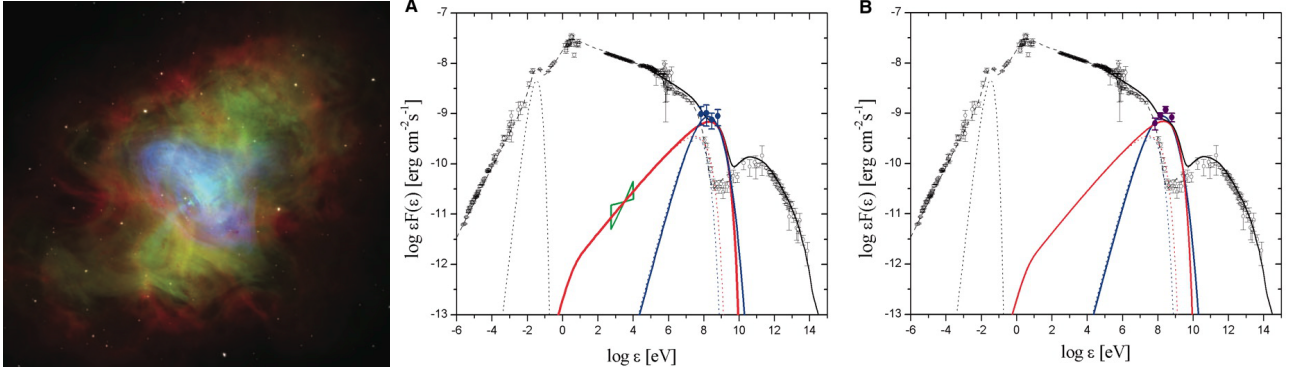
Figure 2.7: Multiwavelength image (left) and spectrum (right) of the Crab pulsar wind nebula. In the image (from [11]): blue colour is X-ray, green is in visible light and red is radio emission. In the spectrum (from [12]) black data points show time-averaged spectrum of the source. Blue and violet points show examples of spectra during GeV band flares.

Measurement of the slope of the synchrotron spectrum provides information on the shape of the parent electron spectrum, which is of a "broken powerlaw" type. Electrons responsible for the emission in the radio-to-visible energy range are characterised by a spectrum with the slope close to $\Gamma_e \simeq 2$, since the synchrotron spectrum has the slope close to $\Gamma_{synch} = 1.5$ (see Eq. (2.64)). One could tentatively interpret this $E^{-2}$ type spectrum either as an un-cooled injection spectrum of electrons, or as a low energy "cooling tail" formed below the low-energy cut-off in the injection spectrum of electrons, see Eq. (2.65).

In the energy range above 10 eV and up to the multi-MeV range the slope of the synchrotron spectrum is close to $\Gamma_{synch} = 2$, so that the slope of the parent electron spectrum is close to $\Gamma_e \simeq 3$. The change of the slope from $\Gamma_e \simeq 2$ at lower energies to $\Gamma_e \simeq 3$ at higher energies might be conveniently interpreted as the effect of synchrotron cooling on the initial electron injection spectrum $\Gamma_{inj} = 2$, since the cooling results in a softening of the spectrum by $\Delta\Gamma_e = 1$ (see Eq. (2.66)). The "cooling break" in the spectrum of electrons, by $\Delta\Gamma_e = 1$ occurs at the energy at which the cooling time is approximately equal to the time since the start of injection of high-energy electrons. Electrons with energies lower than the break energy did no have time to loose their energy since the beginning of injection and their spectrum is the unchanged injection spectrum.

Let us assume that the break observed in the spectrum of synchrotron emission in the Crab nebula is due to the "cooling break' in the spectrum of electrons. The time passed since the start of injection in the nebula is the age of the system, which is about $10^3$ yr (i.e. the time since the supernova explosion which led to formation of the system). The synchrotron cooling time is given by Eq. (2.62):

$$t_{synch} \simeq 10^3 \left[ \frac{B}{100 \ \mu G} \right]^{-2} \left[ \frac{E_e}{10^{12} \ eV} \right]^{-1} \ yr \qquad (2.67)$$

Thus, an estimate of the cooling time provides a constraint on the energy of electrons responsible for the synchrotron emission in the 1-10 eV range and the strength of magnetic field in the nebula. The energy of synchrotron photons is also determined by the energy of electrons and the strength of the magnetic field, but in a different combination, see Eq. (2.60):

$$\epsilon_{synch} \simeq 5 \left[ \frac{B}{100 \ \mu G} \right] \left[ \frac{E_e}{10^{12} \ eV} \right]^2 \ eV \qquad (2.68)$$

combining the two measurements (of $\epsilon_{synch}$ and $t_{synch}$) we find that if the break in the spectrum of synchrotron emission from the Crab nebula is due to the synchrotron cooling effect on electron

spectrum, the magnetic field in the nebula should be close to

$$B \sim 100 \ \mu G \tag{2.69}$$

The energies of electrons for which the cooling time is about the age of the Crab nebula are

$$E_{e,break} \sim 10^{12} \ \text{eV} \tag{2.70}$$

From Fig. (2.7) one could see that the spectrum of synchrotron emission has a high-energy cut-off in the 100 MeV range, where is sharply declines. Electrons which produce synchrotron emission in the 100 MeV energy range should have energies (see Eq. (2.68))

$$E_{e,max} \sim 1 - 10 \ \text{PeV} \tag{2.71}$$

range. This shows that Crab nebula hosts a remarkably powerful particle accelerator. For comparison, the energies of particles accelerated in the most powerful man-made accelerator machine, the Large Hadron Collider, are in the 10 TeV range, which is three orders of magnitude lower.

Up to recently, Crab Nebula was believed to be a non-variable source and was conventionally used as a calibration sources for X-ray and $\gamma$-ray telescopes, due to its high flux and stability. However, recent observations by *Fermi* and *AGILE* $\gamma$-ray telescopes have revealed variability of the $\gamma$-ray emission from Crab, in the form of short powerful flares, during which the GeV flux of the source rises by an order of magnitude, see Fig. 2.7. These flares occur at the highest energy end of the synchrotron spectrum and have durations in the $t_{flare} \sim 1 - 10 \ \text{d} \sim 10^5 - 10^6$ s range. Comparing the synchrotron cooling times of the 1-10 PeV electrons with the duration of the flares, one finds

$$t_{synch} \simeq 24 \left[ \frac{B}{100 \ \mu G} \right]^{-2} \left[ \frac{E_e}{10^{16} \ \text{eV}} \right]^{-1} \ \text{d} \geq t_{flare} \tag{2.72}$$

This implies that the flares occur in the innermost part of the nebula, in the regions with higher magnetic field ($B \sim 500 \ \mu G$), otherwise, long synchrotron cooling time would smooth the flare lightcurve on the time scale $t_{synch}$ and the flare would not have 1 d duration.

The flaring time scale is most probably directly related to the time scale of an (uncertain) acceleration process, which leads to injection of multi-PeV electrons in the nebula. We will come back to this issue later on in the discussion of the properties of pulsars and their nebulae.

### 2.6.2   Proton synchrotron emission

In most of the astrophysical examples, synchrotron emission is produced by high-energy electrons. Higher mass of protons, compared to electrons, makes synchrotron emission rather inefficient as an energy loss channel. Indeed, rescaling Eqs. (2.60) and (2.62) by substituting $m_p$ instead of $m_e$, we find, for the magnetic field in the Crab Nebula

$$\epsilon_{synch,p} = \frac{eBE_e^2}{m_p^3} \simeq 10^{-1} \left[ \frac{B}{10^{-4} \ \text{G}} \right] \left[ \frac{E_e}{10^{16} \ \text{eV}} \right]^2 \text{eV} \tag{2.73}$$

$$t_{synch,p} = \frac{E_e}{-dE_e/dt} = \frac{3m_p^4}{2e^4 B^2 E_e} \simeq 10^{12} \left[ \frac{B}{10^{-4} \ \text{G}} \right]^{-2} \left[ \frac{E_e}{10^{16} \ \text{eV}} \right]^{-1} \text{yr} \tag{2.74}$$

Thus, cooling time of protons with 10 PeV energy (comparable to that of electrons) in the Crab Nebula is, in fact, larger than the age of the Universe, so that the synchrotron energy loss is completely unimportant for them.

Nevertheless, proton synchrotron emission could be an important energy loss mechanism for Ultra-High-Energy Cosmic Ray (UHECR) protons, if they are accelerated in regions with strong magnetic

field, like e.g. the field near supermassive black holes in the AGN, $B \sim 10^4$ G. In this case, the synchrotron loss time is

$$t_{synch,p} = \frac{E_e}{-dE_e/dt} = \frac{3m_p^4}{2e^4B^2E_e} \simeq 3 \left[\frac{B}{10^4 \text{ G}}\right]^{-2} \left[\frac{E_e}{10^{19} \text{ eV}}\right]^{-1} \text{ s} \tag{2.75}$$

which is shorter than the time in which proton crosses the region of the size about the black hole horizon

$$t_{BH} = R_{BH}/c = G_N M_{BH} \sim 30 \left[\frac{M}{10^7 M_\odot}\right] \text{ s} \tag{2.76}$$

If the acceleration process works on the distance scale $R \sim R_{BH}$, proton synchrotron emission is an important energy dissipation mechanism reducing the maximal attainable energies of particles. An observational signature of the efficiently operating proton synchrotron energy loss would be the synchrotron $\gamma$-ray emission from black holes working as particle accelerators. The emission is expected in the energy range

$$\epsilon_{synch,p} = \frac{eBE_e^2}{m_p^3} \simeq 10^{13} \left[\frac{B}{10^4 \text{ G}}\right] \left[\frac{E_e}{10^{19} \text{ eV}}\right]^2 \text{ eV} \tag{2.77}$$

i.e. in the very-high-energy $\gamma$-ray band.

Inspection of an example $\gamma$-ray emission spectrum of a nearby active supermassive black hole in the centre of M87 galaxy, from Fig. 2.4 shows that the $\gamma$-ray spectra of supermassive black holes extend into the $E \sim 10^{13}$ eV energy range. Thus, it is possible that UHECR acceleration process is on-going near these black holes and the observed radiation is produced via synchrotron emission from UHECR protons.
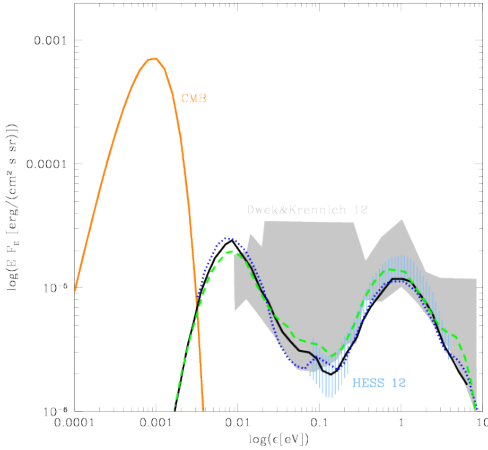
## 2.7   Compton scattering



Figure 2.8: The spectrum of Extragalactic Background Light. Grey band shows the range of uncertainties of currently existing measurements.

The spectrum of emission from the Crab nebula has apparently two "bumps": one starting in the radio band and ending in the GeV band and the other spanning the 10 GeV-100 TeV needy range with a peak in at $\sim 100$ GeV. We have interpreted the radio-to-$\gamma$-ray bump as being the result of synchrotron emission from high-energy electrons in the source. The synchrotron emission is an "inevitable" radiative loss channel in a wide range of astronomical sources, because most of the known sources possess magnetic fields. There is practically no place in the Universe without magnetic field.

Similarly to magnetic fields, the whole Universe is also filled with radiation fields. Radiation was generated by the hot Early Universe. This relic radiation survives till today in the form of Cosmic Microwave Bakcground (CMB). CMB is thermal radiation with temperature $T_{CMB} \simeq 2.7$ K and its present in equal amounts everywhere in the Universe. The spectrum of CMB is the Planck spectrum. Its energy density is

$$U_{CMB} = \frac{\pi^2}{15}T^4 \simeq 0.25 \left[\frac{T_{CMB}}{2.7 \text{ K}}\right]^4 \frac{\text{eV}}{\text{cm}^3} \tag{2.78}$$

and the number density of CMB photons is

$$n_{CMB} = \frac{2\zeta(3)}{\pi^2}T^3 \simeq 4 \times 10^2 \left[\frac{T_{CMB}}{2.7 \text{ K}}\right]^3 \frac{\text{ph}}{\text{cm}^3} \tag{2.79}$$

Apart from the universal CMB photon background, radiation fields are generated by collective emission from stars and dust in all galaxies over the entire galaxy evolution span. This leads to production of the so-called "Extragalactic Background Light" with a characteristic two-bump spectrum shown in Fig. 2.8. The bump at the photon energy $\sim 1$ eV is produced by the emission form stars, the bump at $10^{-2}$ eV is due to the scattering of starlight by the dust. Fig. 2.8 shows the level of the starlight and dust emission averaged over the entire Universe. Inside the galaxies, the densities of both the starlight and dust photon fields are enhanced by several orders of magnitude.

Still denser photon fields exist inside astronomical sources, e.g. close to the stars or in the nuclei of active galaxies.

High-energy particles propagating through the photon backgrounds could occasionally collide with the low energy photons and loose / gain energy in the scattering process. This phenomenon is called Compton scattering.

The high-energy bump in the spectrum of Crab nebula is produced by a variety of the Compton scattering process in which high-energy electrons collide with low energy photons present in the nebula. This results in the transfer of energy from electrons to photons so that the low-energy photons are converted into high-energy $\gamma$-rays and electrons loose their energy. This process is called "inverse Compton scattering". In this section we consider different aspects of the Compton scattering process.

## 2.7.1 Thomson cross-section

The process of charged particle – photon scattering could be described within classical mechanics as re-radiation of waves by the particle accelerated by the electric field of the incident electromagnetic wave.

As an initial example, we consider this process for a non-relativistic electron. The force acting on the charged particle is the Lorentz force

$$\vec{F} = e(\vec{E} + [\vec{v} \times \vec{B}]) \tag{2.80}$$

The wave has electric and magnetic fields of comparable strength. This means that the term proportional to the magnetic field in the Lorentz force is much smaller than the electric field term, because we consider $v \ll 1$. Let us consider the wave propagating in $z$ direction, so that the electric and magnetic field vectors are in the $xy$ plane. The components of acceleration of the particle are

$$a_x \simeq \frac{e}{m} E_x$$
$$a_y \simeq \frac{e}{m} E_y \tag{2.81}$$

For a linearly polarised plane wave, the electric field components at a given position vary as

$$E_x = E_0 \sin(\omega t + \phi) \tag{2.82}$$

where $\omega$ is the wave angular frequency. Thus, $a_x$ oscillates periodically.

Using the Larmor formula, we find the power of emission by the accelerated particle

$$\left\langle \frac{d\mathcal{E}}{dt} \right\rangle = \frac{2}{3} e^2 \left\langle a_x^2 \right\rangle = \frac{2}{3} \frac{e^4}{m^2} \left\langle E_x^2 \right\rangle \tag{2.83}$$

(we introduce curly font for the emitted energy, to avoid confusion with electric field). Time averaged emission power depends on

$$\left\langle E_x^2 \right\rangle = \frac{\omega}{2\pi} \int_0^{2\pi/\omega} E_0^2 \sin^2(\omega t + \phi) dt = \frac{2E_0^2}{\pi} \int_0^{\pi/2} \sin^2 x \, dx = \frac{E_0^2}{2} \tag{2.84}$$

Substituting into Eq. (2.83 we find

$$\left\langle \frac{d\mathcal{E}}{dt} \right\rangle = \frac{1}{3} \frac{e^4}{m^2} E_0^2 \tag{2.85}$$

In scattering theory, the cross-section is defined as the ratio of the emitted energy to the incident energy flux $\vec{S}$

$$\sigma = \frac{d\mathcal{E}/dt}{|\vec{S}|} \tag{2.86}$$

The energy flux of the incident wave is given by the Poynting vector

$$\left\langle \vec{S} \right\rangle = \frac{\left\langle \vec{E} \times \vec{B} \right\rangle}{4\pi} = \frac{E_0^2}{8\pi} \tag{2.87}$$

substituting this into expression for the cross-section we find

$$\sigma = \frac{d\mathcal{E}/dt}{|\vec{S}|} = \frac{8\pi}{3} \frac{e^4}{m^2} \tag{2.88}$$

If the scattering centre is an electron, $e$ is the electron charge and $m = m_e$ is its mass. In this case the cross-section is a fundamental constant called Thomson cross-section:

$$\sigma_T = \frac{8\pi e^4}{3m_e^2} \simeq 6.65 \times 10^{-25} \text{ cm}^2 \tag{2.89}$$

The combination of fundamental constants

$$r_e = \frac{e^2}{m_e} \simeq 3 \times 10^{-13} \text{ cm} \tag{2.90}$$

is called classical electron radius. It also usually enters the tables of fundamental constants. The Thomson cross-section is then

$$\sigma_T = \frac{8\pi}{3} r_e^2 \tag{2.91}$$

that is, the scattering cross-section is close to the "geometrical" cross-section of a disk with the radius equal to the classical electron radius.

Using the definition of $\sigma_T$ one could rewrite the expression for the power of emission as

$$\frac{d\mathcal{E}}{dt} = \frac{8\pi e^4}{3m_e^2} \frac{E_0^2}{8\pi} = \sigma_T U_{rad} \tag{2.92}$$

where we have introduced the notation for the energy density of the incident radiation

$$U_{rad} = \left\langle \frac{\vec{E}^2}{8\pi} + \frac{\vec{B}^2}{8\pi} \right\rangle = \frac{E_0^2}{8\pi} \tag{2.93}$$

### 2.7.2  Example: Compton scattering in stars. Optical depth of the medium. Eddington luminosity

The most widespread example of Compton scattering in astronomy is the scattering of photons inside stars. The nuclear reactions which power stellar activity proceed most efficiently deep in the stellar cores, where temperatures are significantly higher than at the stellar surface. However, we are not able to observe directly radiation from the nuclear reactions, because the star is "opaque" to the radiation. The process which prevents photons produced deep inside the stars from escaping is the Compton scattering.

Let us take the Sun as an example. The average density of the Sun is

$$n_\odot = \frac{M_\odot}{(4\pi/3)R_\odot^3 m_p} \simeq 10^{24} \text{ cm}^{-3} \tag{2.94}$$

From the definition of the scattering cross-section, we find that the mean free path of photons with respect to collisions with electrons inside the Sun is just

$$\lambda = \frac{1}{\sigma_T n_\odot} \simeq 1 \text{ cm} \tag{2.95}$$

This mean free path is much shorter than the distance of the order of the size of the Sun $R_\odot \simeq 7 \times 10^{10}$ cm which the photon needs to cross before leaving the surface of the Sun. Since $\lambda \ll R_\odot$, none of the photons produced in the core is able to escape. The source is opaque to photons. The opacity of the source of the size $R$ is often measured in terms of the optical depth, which is, by definition

$$\tau = \frac{R}{\lambda} \tag{2.96}$$

In the case of the Sun we find that $\tau \sim 10^{11}$. The optical depth also describes the law of attenuation of a directed beam of photons (or of any other particles) by the scattering in the medium. The number of particles in the beam in $z$ direction entering the medium at $z = 0$ decreases with distance as

$$N(z) = N_0 \exp\left(-\tau(z)\right), \tau(z) = \frac{z}{\lambda} \tag{2.97}$$

If we assume that Compton scattering results in random changes of the direction of motion of photons, we could describe the process of escape of photons from inside the star as a random walk or diffusion in 3d space. The law of diffusion allows to estimate the time needed for photons to escape from the core

$$t = \frac{R^2}{\lambda} = \tau \frac{R}{c} \simeq 10^{11} \text{ s for the Sun} \tag{2.98}$$

Thus, Compton scattering slows down the radiative transfer from the core to the surface of the stars.

Compton scattering is important in stars in still another aspect. Compton scattering of photons on electrons results in energy transfer between the two particles. In this way a flux of radiation from a given direction produces pressure on the plasma (radiation pressure). If we imagine a low energy photon bouncing from an electron, the change of momentum of the photon in result of scattering is about the momentum itself, $\Delta p \sim p \sim \epsilon$, where $\epsilon$ is the photon energy. A flux of photons with density $n$ transfers an energy to each electron in the plasma at a rate comparable to the power of the scattered radiation

$$\frac{d\mathcal{E}}{dt} \simeq \epsilon n \sigma_T \tag{2.99}$$

This energy transfer is the result of action of the radiation force $d\mathcal{E} = F_{rad}dt$.

Sun-like stars are supported by the balance of gravity force and pressure of the stellar plasma. However, in massive stars with much higher luminosity than that of the Sun, the force due to the radiation pressure competes with the gravity and the equilibrium configuration of the star is supported by the balance of gravity and radiation pressure force

$$\frac{G_N M m_p}{R^2} \simeq \epsilon n \sigma_T \tag{2.100}$$

(we assume that the number of protons and electrons in the star is the same). The strongest radiation pressure force is acting on electrons, stronger gravity force is acting on protons. Expressing the density of radiation through the luminosity $L$

$$\epsilon n = \frac{L}{4\pi R^2} \tag{2.101}$$

and substituting into above equation we find an expression for $L$ through the mass of the star

$$L_{Edd} = \frac{4\pi G_N M m_p}{\sigma_T} \simeq 10^{38} \left[ \frac{M}{M_\odot} \right] \text{ erg/s} \tag{2.102}$$

This mass-dependent luminosity, called Eddington luminosity, is, in fact an upper limit on the luminosity of a self-gravitating object. No persistent astronomical source of the mass $M$ could have luminosity higher than $L_{Edd}$, because otherwise the source would be disrupted by the radiation pressure force. This limit applies not only to the stars, but also for numerous other source types and we will see several examples of the use of the Eddington limit later on in the course.

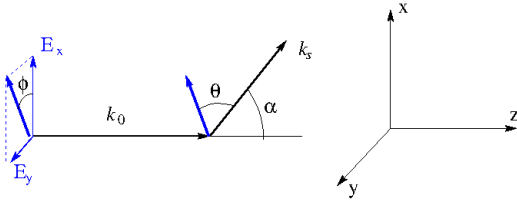### 2.7.3   Angular distribution of scattered waves



Figure 2.9: Geometry of Compton scattering.

The angular distribution of the waves emitted by a non-relativistic scattering centre could be found from a general formula for the dipole radiation from non-relativistic particle (2.9)

$$\frac{d\mathcal{E}}{dt d\Omega} = \frac{e^2}{4\pi} |a|^2 \sin^2\theta \tag{2.103}$$

where $\theta$ is the angle between the direction of acceleration and the direction of the scattered wave. To calculate this angle, we choose the coordinate system in the following way (see Fig. 2.9). The $z$ axis points in the direction of the incident wave. The $xz$ plane contains the wave vector of the incident wave, $\vec{k}_0$ and the wave vector of the scattered wave, $\vec{k}_s$. The $y$ axis is orthogonal to the $xz$ plane. In such notations we rewrite the above equation as

$$\frac{d\mathcal{E}}{dt d\Omega} = \frac{e^2}{4\pi} \left| \vec{a} \times \vec{k}_s \right|^2 = \frac{e^4}{4\pi m^2} \left| \vec{E} \times \vec{k}_s \right|^2 = \frac{e^4}{4\pi m^2} \left| (\vec{E}_x + \vec{E}_y) \times \vec{k}_s \right|^2 \tag{2.104}$$

where $\vec{E}_x, \vec{E}_y$ are components of the electric field along x and y axes. The vector $\vec{E}_x \times \vec{k}_s$ is directed along the $y$ axis, while the vector $\vec{E}_y \times \vec{k}_s$ lies in the $xz$ plane. They are orthogonal to each other. This implies that the square of the norm of their sum is the sum of their norms square

$$\frac{d\mathcal{E}}{dt d\Omega} = \frac{e^4}{4\pi m^2} \left( \left| \vec{E}_x \times \vec{k}_s \right|^2 + \left| \vec{E}_y \times \vec{k}_s \right|^2 \right) \tag{2.105}$$

$\vec{E}_y$ is orthogonal to $\vec{k}_s$, so that their vector product is just the product of the norms

$$\left\langle \left| \vec{E}_y \times \vec{k}_s \right|^2 \right\rangle = \frac{1}{2} E_{0,y}^2 \tag{2.106}$$

where we have used the fact that the time averaging of the electric field norm square results in the factor $1/2$ (see Eq. (2.84)). Introducing the angle $\alpha$ between the direction of the incident and scattered wave, one could find that $\theta = \pi/2 - \alpha$. Thus

$$\left\langle \left| \vec{E}_x \times \vec{k}_s \right|^2 \right\rangle = \frac{1}{2} E_{0,x}^2 \cos^2\alpha \tag{2.107}$$

Let us assume that the incident wave is unpolarised, so that $E_{0,x} \simeq E_{0,y} \simeq E_0/\sqrt{(2)}$ for any choice of the scattering direction $\vec{k}_s$. Then we could add the two terms together to find

$$\frac{d\mathcal{E}}{dt d\Omega} = \frac{e^4 E_0^2}{16\pi m^2} \left( 1 + \cos^2\alpha \right) \tag{2.108}$$

Division by the energy flux of the incident wave gives the differential cross-section of Compton scattering

$$\frac{d\sigma}{d\Omega} = \frac{d\mathcal{E}/(dt\,d\Omega)}{S} = \frac{e^4}{2m^2}(1+\cos^2\alpha) \qquad (2.109)$$

As a verification, we could find that integrating the differential cross-section over the solid angle gives the Thomson cross-section

$$\int d\Omega \frac{d\sigma}{d\Omega} = \sigma_T \qquad (2.110)$$

For a polarised wave, the amplitude of Compton scattering depends not only on the angle $\alpha$, but also on the azimuthal angle $\phi$, since $\theta$ is a function of both $\alpha$ and $\phi$. This fact could be used to measure the polarisation of the incident radiation. It is indeed used in telescopes for this purpose. An example of a "gamma-ray polarimeter" based on this principle is given by POLAR detector for the measurement of polarisation of Gamma-ray bursts. We will stop at this issue in a subsection discussing Compton telescopes later on.
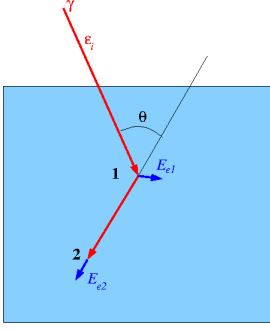
### 2.7.4 Thomson scattering

To find the energy transfer from electron to photon or vise versa we write down the energy-momentum conservation law

$$\underline{p}_{e,i} + \underline{p}_{\gamma,i} = \underline{p}_{e,f} + \underline{p}_{\gamma,f} \qquad (2.111)$$

where the subscripts $e, \gamma$ refer to electron and photon and $i, f$ are for initial and final state. We could re-express this as



Figure 2.10: Principle of operation of Compton telescope

$$m_e^2 = |p_{e,f}|^2 = (\underline{p}_{e,i} + \underline{p}_{\gamma,i} - \underline{p}_{\gamma,f})^2 = m_e^2 + 2(\underline{p}_{e,i}\underline{p}_{\gamma,i} - \underline{p}_{e,i}\underline{p}_{\gamma,f} - \underline{p}_{\gamma,i}\underline{p}_{\gamma,f}) \qquad (2.112)$$

Let us consider the system of reference where the electron is initially at rest, that is $\underline{p}_{e,i} = (m_e, 0, 0, 0)$ in components. We could choose the $x$ axis along the initial direction of motion of photon in this system so that $\underline{p}_{\gamma,i} = \epsilon_i(1, 1, 0, 0)$. Then we choose the $y$ axis orthogonal to $x$ in the plane of scattering, so that $\underline{p}_{\gamma,f} = \epsilon_f(1, \cos\theta, \sin\theta, 0)$, where we have introduced the initial and final energies of the photon, $\epsilon_i, \epsilon_f$ and the scattering angle $\theta$. Substituting the component in the last equation we find

$$m_e\epsilon_i = m_e\epsilon_f + \epsilon_i\epsilon_f(1 - \cos\theta) \qquad (2.113)$$

or, reexpressing $\epsilon_f$,

$$\epsilon_f = \frac{\epsilon_i}{1 + \frac{\epsilon_i}{m_e}(1 - \cos\theta)} \qquad (2.114)$$

For example, for the scattering at zero angle $\theta = 0$ we find



Figure 2.11: Cross-section of interaction of photons with medium (Germanium) as a function of energy.

that there is no energy transfer between electron and photon: $\epsilon_i = \epsilon_f$. For the scattering at $\theta = \pi$ we have $\epsilon_f = \epsilon_i/(1 + 2\epsilon_i/m_e) < \epsilon_i$. In this case the energy of photon is used on the recoil of electron.

Scattering of low energy photons by non-relativistic electrons is characterised by tiny changes of the photon energy, so that $\epsilon_f \simeq \epsilon_i$. This limits is called Thomson scattering (e.g. close to the surface of the star).
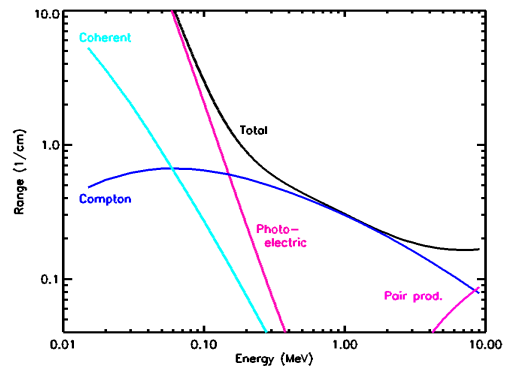
### 2.7.5   Example: Compton telescope(s)

The above Eq. (2.114) is the main ingredient in the principle of operation of the so-called Compton telescopes, i.e. telescopes which detect $\gamma$-rays though the Compton scattering effect. Imagine a setup in which a moderate energy $\gamma$-ray enters a detection volume and scatters on an electron at a point 1 as shown in Fig. 2.10.

The $\gamma$-ray transfers a part of its energy $E_{e1} = \epsilon_f - \epsilon_i$ to an electron. Depending on the choice of the detection medium, the energy of electron can be measured in a variety of ways. For example, if the medium is a scintillator, the scintillation signal could be sampled by photomultiplier sensors. Otherwise, if the medium is a semiconductor, electron excitation will lead to production of electron-hole pairs which could then be sampled in the form of a current flowing through an electric circuit including the detector.

The scattered photon continues its path an could interact second time inside the detector medium at the point 2. The energy of the scattered photon $\epsilon_f$ is lower than $\epsilon_i$ and the second interaction could, with a good chance, be photoelectric absorption, rather than Compton scattering. This is because the Compton scattering dominates the photon-medium interaction cross-section only in a narrow energy interval from $\epsilon_i \sim 100$ keV to about the rest energy of electron, $\epsilon_i \sim m_e = 511$ keV. At lower energies $\epsilon_i \lesssim 100$ keV the highest interaction cross-section is that of the photoelectric effect, see Fig. 2.11 for an example of the Germanium (semiconductor) detection medium.

Photoelectric absorption also transfers the photon energy to (another) which gets the energy $E_{e2} = \epsilon_f$. Measuring $E_{e2}$ in the same way as $E_{e1}$ one could constrain parameters of Compton scattering at point 1. Indeed, the unknown parameters are the photon energy $\epsilon_i$ and the scattering angle $\theta$. Measuring $E_{e2} = \epsilon_f$ and $E_{e1} = \epsilon_i - \epsilon_f$ one could find both $\epsilon_i$ and $\theta$ from Eq. (2.114).

Knowing the scattering angle $\theta$ and the direction of the line from point 1 to point 2, one could reconstruct the initial photon direction, provided that the scattering plane is well constrained. Otherwise, in the absence of information on the orientation of the plane of scattering, there remains a residual uncertainty in the direction of the initial photon: it could come anywhere from a cone with the axis along 1-2 direction and the opening angle $\theta$. The orientation of the plane of scattering could, in principle, be constrained if the direction of motion of the electron scattered at point 1 is measured. However, this is usually challenging because the electron immediately experiences miltiple scattering in the detector volume and quickly looses the "memory" of its initial direction. In this way, the measurements of the directions of photons detected by Compton telescopes are usually not spots on the sky, but rather "rings on the sky".



Figure 2.12: COMPTEL telescope which was operational on Compton Gamma-Ray Observatory

The only space-based Compton telescope which was operational up to now was COMPTEL on board of Compton Gamma-Ray Observatory mission by NASA. It was operation in the 90th of the last century. The setup of the telescope is shown in Fig. 2.12. In the COMPTEL setup the "scatterer" and "absorber" detectors (containing, respectively, the scattering point 1 and the absorption point 2) were separated by a distance of about 1 m onto two sub-detectors. Both sub-detectors were scintillators (liquid scintillator for the scatterer and NaI crystals for the lower absorber detector). The large separation between the sub-detectors was necessary for suppression of the background of up-going particles from the direction of the Earth. The up-going particles were rejected based on the "time-of-flight" measurement principle: they produced first signal in the "absorber" and second signal in the "scatterer", while the $\gamma$-rays from the sky produced first the signal in the "scatterer" and then in the "absorber".
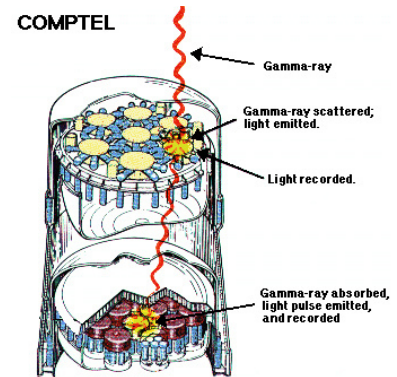
    The separation of the two detectors, although useful for the background rejection, strongly reduced the efficiency of the telescope. Large fraction of the scattered $\gamma$-rays just did not arrive at the lower detector. Because of this, COMPTEL had a limited sensitivity and detected only about 10 sources on the sky. Our lack of sensitive instruments (and knowledge) in the MeV energy domain is known as the "MeV sensitivity gap". Telescopes operating in adjacent energy bands (below 100 keV and above 100 MeV are much more sensitive and our knowledge of the sky in those energy bands is much more complete.

## 2.8   Inverse Compton scattering

Up to now we have considered scattering of photons by electron at rest. In this case it is the photon which transfers a fraction of its energy to electron. If electrons are moving, opposite is also possible: electron could transfer a fraction of its energy to photon. In this case Compton scattering works as a radiative energy loss for high-energy electrons. This process is called inverse Compton scattering. Below we derive necessary formulae describing this radiative energy loss.

### 2.8.1   Energies of upscattered photons

The case of arbitrary initial four-momentum of electron could be reduced to the case of electron in rest via a transformation to the coordinate system comoving with the electron. Suppose that electron moves with velocity $v$ along $x$ axis in the "lab" frame. In the same frame photon moves at an angle $\theta_0$ w.r.t. electron and its four-momentum is $\underline{p}_{\gamma,i} = \epsilon_i(1, \cos\theta_0, \sin\theta_0, 0)$. Lorentz transformation of photon four-momentum to the electron comoving frame changes the energy as

$$\tilde{\epsilon}_i = \epsilon_i \gamma (1 - v \cos\theta_0) \tag{2.115}$$

where $\gamma$ is the Lorentz factor of electron. The final energy of scattered photon in the comoving frame is

$$\tilde{\epsilon}_f = \frac{\tilde{\epsilon}_i}{1 + \frac{\tilde{\epsilon}_i}{m_e}(1 - \cos\theta)} \tag{2.116}$$

where $\theta$ is the scattering angle in the comoving frame. The final photon energy in the lab frame is related to $\tilde{\epsilon}_f$ also via Lorentz transformation

$$\epsilon_f = \tilde{\epsilon}_f \gamma (1 + v \cos\theta_f) = \frac{\epsilon_i \gamma^2 (1 - v\cos\theta_0)(1 + v\cos\theta_f)}{1 + \frac{\tilde{\epsilon}_i}{m_e}(1 + \cos\theta)} \tag{2.117}$$

where $\theta_f$ is the angle of outgoing photon w.r.t. the $x$ axis in the comoving frame.

    Now let us consider situation in which the energy of the incident photon in the electron comoving frame is small

$$\tilde{\epsilon}_i \ll m_e \tag{2.118}$$

For this to be true we have to require

$$\epsilon_i \gamma (1 - v \cos\theta_0) \ll m_e \tag{2.119}$$

which, by itself requires

$$\epsilon_i E_e \ll m_e^2 \tag{2.120}$$

where $E_e = \gamma m_e$ is the initial electron energy. Compton scattering of low-energy photons by relativistic electrons in the regime where low-energy photons satisfy condition (2.120) is called "inverse Compton scattering in Thomson regime".

In this case Eq. (2.117) simplifies and we find

$$\epsilon_f \simeq \epsilon_i \gamma^2 (1 - v \cos \theta_0)(1 + v \cos \theta_f) \tag{2.121}$$

Now assume that the low energy photons form an isotropic radiation field and the angle $\theta_0$ is random. In the electron comoving frame, the scattering amplitude is comparable in all the directions, so that the angle $\theta_f$ also takes arbitrary values. This means that a good estimate of the average final energy of photons is

$$\epsilon_f \simeq \epsilon_i \gamma^2 \simeq 3 \left[ \frac{\epsilon_i}{1 \text{ eV}} \right] \left[ \frac{E_e}{10^{10} \text{ eV}} \right]^2 \text{ GeV} \tag{2.122}$$

Thus, contrary to the scattering of waves on electron at rest, where the scattering process took the energy from the wave, here the energy is transferred from electron to photons and the process converts low energy photons into high energy $\gamma$-rays. Such process is called "inverse" Compton scattering.

Note that as long as condition (2.120) is satisfied, the final energy of photons $\epsilon_f$ is always

$$\epsilon_f \ll E_e \tag{2.123}$$

At each scattering event electron transfers only a small fraction of its energy to the photon.

The scattering angle is approximately arbitrary in the comoving frame. However, in the lab frame the scattering would appear strongly beamed in forward direction, within a cone with an opening angle $\gamma^{-1}$.

## 2.8.2   Energy loss rate of electron

To calculate the energy loss rate of electron due to the inverse Compton scattering of low energy photons, we could use the non-relativistic result which is valid in the frame comoving frame

$$\frac{d\tilde{\mathcal{E}}}{d\tilde{t}} = \sigma_T \tilde{U}_{rad} \tag{2.124}$$

Actually, the same result should hold also in the lab frame since $dt$ and $E$ are both 0th components of covariant four vectors and transform identically under Lorentz transformation. In this frame it would express the energy carried away by the radiation

The r.h.s. of Eq. (2.124) contains the energy density of radiation in the comoving frame, $\tilde{U}_{rad}$. To express this quantity in the lab frame, one could notice that the density of photons $n(\epsilon)$ also transforms under Lorentz transformation in the same way as $dt$, because the number of photon in a given volume element $n(\epsilon)d^3x$ is a relativistic invariant as well as the four-volume element $dt d^3x$. Thus, using Eq. (2.115) the density of photons in the comoving frame could be expressed through the density in the lab frame as

$$\tilde{n} = n\gamma(1 - v \cos \theta_0) \tag{2.125}$$

The energy density of photons is

$$\tilde{U}_{rad} = \tilde{\epsilon}\tilde{n} = \epsilon n \gamma^2 (1 - v \cos \theta_0)^2 \tag{2.126}$$

and

$$\frac{d\mathcal{E}}{dt} = \sigma_T U_{rad} \gamma^2 (1 - v \cos \theta_0)^2 \tag{2.127}$$

If the low energy photon field is isotropic, we could find average energy loss rate into radiation by averaging over the angle $\theta_0$ which gives

$$\frac{d\mathcal{E}}{dt} = \frac{4}{3} \sigma_T U_{rad} \left( \gamma^2 - \frac{1}{4} \right) \tag{2.128}$$

The energy loss of electron is the energy carried away by electron minus the initial energy of photon field passing by electron every second, $\sigma_T U_{rad}$. Subtracting this from the above expression we find

$$\frac{d\mathcal{E}_e}{dt} = \frac{4}{3}\sigma_T U_{rad}(\gamma^2 - 1) = \frac{4}{3}\sigma_T U_{rad}\gamma^2\beta^2 \tag{2.129}$$

Similarly to the previously considered cases of synchrotron and curvature energy losses, it is useful to introduce the inverse Compton cooling time via a relation

$$t_{IC} = \frac{E_e}{dE_e/dt} = \frac{3}{4}\frac{m_e^2}{\sigma_T U_{rad}\beta^2 E_e} \simeq 3 \times 10^7 \left[\frac{U_{rad}}{1 \text{ eV/cm}^3}\right]^{-1} \left[\frac{E_e}{10^{10} \text{ eV}}\right]^{-1} \text{ yr} \tag{2.130}$$

### 2.8.3 Evolution of particle distribution with account of radiative energy loss

Eqs. (2.129), which express the energy loss rate of electron due to a radiative energy loss shows that the scaling of the inverse Compton energy loss with electron energy is

$$\frac{d\mathcal{E}_e}{dt} \sim E_e^2 \sim E_e^\kappa \tag{2.131}$$

with the index $\kappa = 2$, as in the case of synchrotron energy loss. We could directly use the results of sections 2.3 and 2.4 to find the effect of the inverse Compton energy loss on the spectrum of electrons.

Similarly to previously considered cases of curvature and synchrotron radiation, we consider two characteristic examples of the steady-state solution of kinetic equation (2.35), neglecting the escape of particles. The first example is that of the mono energetic injection of electrons at an energy $E_0$, $Q(E) \sim \delta(E - E_0)$. In this case the solution (2.36) of the kinetic equation has the form

$$f_e(E) \sim \begin{cases} E^{-2}, & E < E_0 \\ 0, & E > E_0 \end{cases} \tag{2.132}$$

Symilarly to the case of synchrotron emission, cooling of electrons via inverse Compton scattering process leads to formation of a low-energy powerlaw tail in the electron spectrum, with the slope $E^{-2}$.

Another characteristic example is the case of a powerlaw injection spectrum of electrons, $Q(E) \sim E^{-\Gamma_{inj}}$. In this case the solution (2.36) of the kinetic equation takes the form

$$f_e(E) \sim E^{-(\Gamma_{inj}+1)} \tag{2.133}$$

Again, similarly to the synchrotron emission, inverse Compton cooling leads to a softening of the injection spectrum by $\Delta\Gamma = +1$.

### 2.8.4 Spectrum of emission from a broad-band distribution of particles

Eq. (2.122) provides an expression for the energy of photons produced in a radiative loss process:

$$\epsilon_f \sim E_e^2 \sim E_e^\sigma \tag{2.134}$$

with the index $\sigma = 2$, as in the case of synchrotron radiation. Again, we could re-use the previously derived formulae for the spectrum of emission from a broad distribution of electrons derived in section 2.4.

In this way we find that the spectrum of emission from a powerlaw distribution of electrons $dN_e/dE \sim E^{-\Gamma_e}$ is also a powerlaw with a slope

$$\Gamma = \frac{\Gamma_e + 1}{2} \tag{2.135}$$

### 2.8.5   Example: Very-High-Energy gamma-rays from Crab Nebula

At this point we could come back to the example of the broad band spectrum of the Crab Nebula (see Fig. 2.7). The synchrotron component of the spectrum is cut-off at GeV energy. Above this energy, one could see a gradually rising new component which reaches maximum power in the 100 GeV energy band.

This high-energy component is conventionally attributed to the inverse Compton emission from the same electrons which produce synchrotron emission at lower energies. In section 2.6.1 we have found that the shape of the synchrotron spectrum of the Nebula suggests that the synchrotron emission is produced by electrons forming a broken powerlaw distribution. The break in the electron spectrum at the energy $E_{e,break} \simeq 1$ TeV is the "synchrotron cooling" break. Electrons with higher energies have had enough time to loose their energy via synchrotron radiation, while for electrons of lower energies the cooling time is longer than the age of the source ($10^3$ yr, since the supernova explosion which led to formation of the Crab pulsar). Energies of electrions emitting synchrotron radiation in the 100 MeV – GeV energy band reach $1 - 10$ PeV.

Let us not calculate the properties of inverse Compton emission produced by these electrons. First, we need to understand which low energy photon field provides most of the target photons for inverse Compton scattering. The photon fields present in the Crab nebula include the "universal" soft photon field, the CMB, with the energy density $U_{rad} = 0.25$ eV/cm$^3$. Next, since the source is in the Galaxy, it "bathes" in the interstellar radiation field, produced by stars and dust in the Galaxy. Crab is not far for the Sun ($D_{Crab} \simeq 2$ kpc distance) and one could estimate the density of the interstellar radiation field at the location of the Crab based on the knowledge of the local interstellar radiation field density which is about $U_{rad} \sim 1$ eV/cm$^3$.

Finally, the synchrotron radiation produced by the high-energy electrons in the Crab Nebula also provides abundant target photon field for the inverse Compton scattering. We could estimate the density of this radiation field from the measured flux of Crab (see Fig. 2.7). The flux reaches $F_{crab} \simeq 10^{-7.5}$ erg/cm$^2$s in the visible / IR energy band $\epsilon_{ph} \sim 1$ eV. The size of the innermost part of the Crab Nebula is about $d_{Crab} \simeq 1$ pc. The flux of the photons escaping from the Nebula higher than the flux detected on Earth by a factor $(D_{Crab}/d_{Crab})^2 \sim 4 \times 10^6$. The flux (measured in erg/cm$^2$s) is related to the energy density of radiation as $F_{crab} = U_{rad}c$, so that the energy density of synchrotron radiation could be estimated as

$$U_{rad} = F \left( \frac{D_{Crab}}{d_{crab}} \right)^2 \simeq 3 \frac{\text{eV}}{\text{cm}^3} \tag{2.136}$$

which is somewhat higher than the estimate of the density of the interstellar radiation field and is an order of magnitude higher than the CMB energy density. This means that the main source of the soft photons for inverse Compton scattering in Crab is the synchrotron radiation of the nebula itself.

According to Eq. (2.122), electrons with the energies about $E_{e,break}$ should upscatter the synchrotron photons with energies $\epsilon_{ph} \simeq 1$ eV up to the energy $E_\gamma \simeq 10^{14}$ eV, which is, obviously, not possible because the energy of $\gamma$-ray could not exceed the energy of electron. This means that the condition (2.120) in which the Eq. (2.122) is not satisfied for electrons of such high energy. Instead, the inequality (2.120) is saturated already at the energy

$$E_e \simeq \frac{m_e^2}{\epsilon_{ph}} \simeq 2.5 \times 10^{11} \left[ \frac{\epsilon_{ph}}{1 \text{ eV}} \right]^{-1} \text{eV} \tag{2.137}$$

This is exactly the energy at which the maximum of the power of inverse Compton emission is reached, see Fig. 2.7.

### 2.8.6   Inverse Compton scattering in Klein-Nishina regime

From Figure 2.7 one could find (within the considered model of electron spectrum) that the power of inverse Compton energy loss gets suppressed in the regime when $E_e \gg m_e^2/\epsilon_{ph}$, called Klein-Nishina

regime of inverse Compton scattering. In this regime, each scattering event transfers a significant fraction of electron energy to the photon so that $E_\gamma \simeq E_e$. The inverse Compton energy loss time is then just the time between subsequent collisions of electron with photons, which is the interaction time

$$t_{IC,KN} = \frac{1}{\sigma_{KN} n_{ph}} \simeq 10^6 \text{ yr} \left[\frac{\sigma_{KN}}{\sigma_T}\right]^{-1} \left[\frac{n_{ph}}{1 \text{ cm}^{-3}}\right]^{-1} \text{yr} \quad (2.138)$$

It depends on the electron energy, because the cross-section of inverse Compton scattering in this regime $\sigma_{KN}$ is no longer constant.

The exact expression for the cross-section is derived from quantum mechanical treatment of the scattering process. This could be understood after a transformation to the comoving reference frame of electron. In this reference frame, the incident photon has an energy higher than the rest energy of electron $\tilde{\epsilon}_i = x m_e$, $x > 1$. Its wavelength $\lambda \simeq \epsilon_i'^{-1}$ is shorter or comparable to the Compton wavelength of electron, $\lambda_C = 1/m_e$. This means that electron could not be considered anymore as a classical particle influenced by an incident electromagnetic wave.

The quantum mechanical expression for the scattering cross-section is

$$\sigma_{KN} = \frac{3\sigma_T}{8x} \left\{ \left[1 - \frac{2(x+1)}{x^2}\right] \ln(2x+1) + \frac{1}{2} + \frac{4}{x} - \frac{1}{2(2x+1)^2} \right\} \quad (2.139)$$

where $x = \tilde{\epsilon}_i/m_e$ is the incident photon energy in the comoving frame expressed in units of electron energy.

The above expression reduces to $\sigma_T$ in the limit $x \ll 1$. Indeed, expanding the term in the brackets in powers of $x$ we find

$$\{...\} \simeq \left(1 - \frac{2}{x} - \frac{2}{x^2}\right) \left(2x - 2x^2 + \frac{8x^3}{3}\right) + \frac{1}{2} + \frac{4}{x} - \frac{1}{2}(1 - 4x) \simeq \frac{8x}{3} \quad (2.140)$$

In the regime $x \gg 1$, the asymptotic behaviour of the cross-section is

$$\sigma_{KN} \simeq \frac{3\sigma_T}{8} \frac{\ln(2x)}{x} \quad (2.141)$$

The energy of the incident photon in the electron comoving frame is given by Eq. (2.115). It scales as $x = \tilde{\epsilon}_i/m_e \sim \epsilon_i E_e/m_e^2$ with the electron energy. This means that the inverse Compton scattering cross section in Klein-Nishina regime decreases with electron energy as

$$\sigma_{KN} \sim \frac{\ln(E_e)}{E_e} \quad (2.142)$$

in the limit of large $E_e$. This is consistent with the observation done in the previous section, based on the interpretation of inverse Compton emission spectrum of the Crab nebula. Indeed, in the Klein-Nishina regime the inverse Compton cooling time increases with energy as

$$t_{IC,KN} \sim \frac{1}{\sigma_{KN}} \sim \frac{E_e}{\ln(E_e)} \quad (2.143)$$

Thus, the inverse Compton cooling becomes less and less efficient and the power of inverse Compton emission drops at the energies above the Klein-Nishina / Thomson regime transition energy.

Different dependence of the energy of photons on the energy of electrons ($\sigma = 1$ in terms of the powerlaw scaling of Eq. (2.43) and of the cooling rate of electrons on their energy, $dE_e/dt \sim E_e/t_{IC,KN} \sim ln(E_e)$, with $\gamma_{cool} \simeq 0$ in the notations of Eqs. (2.37), (2.39), lead to different slopes of the spectra of emission from a broad band distribution of electrons and to a different effect of cooling on the electron spectrum. From Eq. (2.37) we find that the low energy cooling tail below the energy of injection of electrons $E_0$ is very hard, with the slope $dN_e/dE_e \sim E_e^0$ in this case. In the case of

powerlaw injection spectrum, cooling via inverse Compton scattering in Klein-Nishina regime leads to hardening, rather than softening of the electron spectrum, from the slope $\Gamma_{inj}$ down to the slope with index $\Gamma_{inj} - 1$. The spectrum of inverse Compton photons from a powerlaw distribution of electrons has the same slope as the spectrum of electrons, $\Gamma \simeq \Gamma_e$.

One could also note that the energy of transition between the Thomson and Klein-Nishina regimes of inverse Compton scattering is marked by a change in the slope of the photon spectrum from the slope $(\Gamma_e + 1)/2$ to $\Gamma_e$.

## 2.9  Bethe-Heitler pair production

In the electron rest frame the transition between the Thomson and Klein-Nishina regimes of Compton scattering takes place at the photon energy $E_\gamma \simeq m_e$. The change in the behaviour of Compton scattering cross-section, from nearly constant value $\sigma \simeq \sigma_T$ to a decreasing function of energy $\sigma \sim E^{-1} \ln(E)$ could be seen in Fig. 2.11. On occasion, the figure shows the photon interaction cross-section as a function of energy in silicon, but qualitatively similar picture is seen for any material.

Photon energy range $E_\gamma \sim m_e$ is remarkable also from another point of view. As soon as the energy of the incident photon reaches $2m_e$, the energy transfer in photon-matter collisions becomes sufficient for production of electron-positron pairs. This process is also characterised by a scattering cross-section. The onset of the pair production is seen in Fig. 2.11 as the new (magenta) component of the cross-section appearing at the highest energies. This new cross-section becomes larger than the Compton scattering cross-section already at $E_\gamma \sim 10$ MeV energies (the exact value depends on the material).

In principle, two different processes could contribute to the pair production by a photon propagating through matter. First, photon collision with an electron could lead to a conversion of photon into a pair of electron and positron. The formula of the reaction is then $\gamma + e^- \rightarrow e^- + e^+ + e^-$ and the process is called "triplet production", because there are three electron-like particles at the outcome of reaction. This process is intrinsically a quantum mechanical process and its cross-section is calculated using quantum-
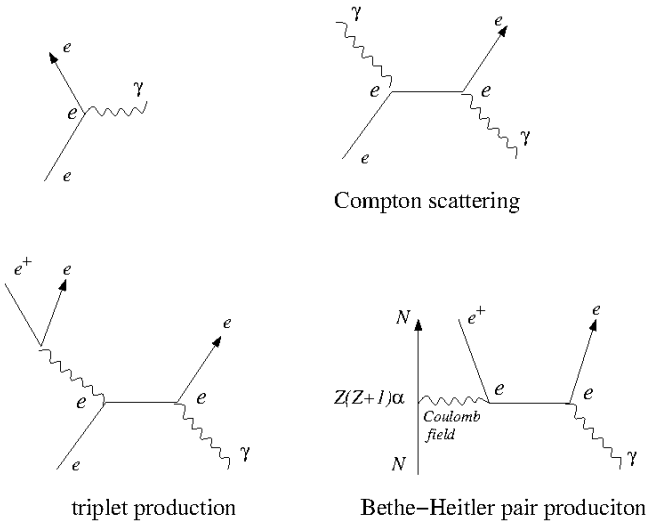


Figure 2.13: Feynman diagrams. Left top: graphical representation of the "vertex" term for electromagnetic interactions. Right top: Feynman diagram of Compton scattering. Left bottom: the diagram of the triplet production. Right bottom: pair production on atomic nucleus (Bethe-Heitler).

mechanical perturbation theory applied for photon-electron scattering (the conventional approach for calculation of scattering amplitudes in Quantum Electrodynamics, QED). The small parameter of the perturbative theory is the interaction strength, or compiling constant. In the case of QED it is the square of particle electric charge. For electron interactions it is the fine structure constant $\alpha = e^2$.

In quantum mechanics the scattering cross-section is given by the square of the absolute value of the scattering amplitude. This scattering amplitude is, in general, a sum of several terms in each order of perturbation theory (terms proportional to some power of $\alpha$). In QED the number of terms entering the sum could be quite large. A convenient way of accounting of all the terms entering the scattering amplitude in a given order of perturbative expansion was introduced by Feynman and is known as "Feynman diagrams" technique.

Each term of the scattering amplitude proportional to $\alpha$ is graphically represented as a vertex

containing two electron "legs" for incoming and scattered electron and one photon (or, more generally, electromagnetic field) leg, as shown in Fig. 2.13. Diagrams in any order of the scattering amplitude for any number of incoming and outgoing particles are composed of a number of vertexes joined by the lines, or "propagators" of free electrons and photons. Each vertex and each line correspond to a particular multiplicative term in the expression for the scattering amplitude. Lines with two ends attached to vertexes correspond to integrals over particle momenta, also present in expressions for the scattering amplitude. The Feynman diagram technique provides an elegant way of encoding of bulky formulae for the scattering amplitudes.

It also provides a qualitative insight into the judgement of relative importance of different interaction "channels". For example, an event of electron-photon collision could have two different outcomes: Compton scattering, in which the photon survives, but its momentum is changed and pair production, in which the photon does not survive and instead an electron-positron pair is produced. It is not clear a-priori, which process is expected to happen more often (i.e. to have larger scattering cross-section).

This becomes clear if one uses the technique of Feynaman diagrams. The diagram for the Compton scattering process has the form shown in the middle of Fig. 2.13, while the diagram for the pair production is on the right of this figure. Once could see that the Compton scattering diagram has two electron-photon vertexes. Thus, it enters the scattering amplitude in the $\alpha^2$ order of perturbation theory. To the contrary, the pair production diagram has three electron-photon vertexes. This means that the contribution of this process into the electron-photon scattering amplitude enters the $\alpha^3$ terms. Thus, the order of magnitude estimate of the scattering cross-section of the pair production is by a factor of $\alpha = \simeq 0.007$ smaller than that of the Compton scattering. The pair production could start to compete with Compton scattering only deep in the Klein-Nishina regime when the Compton scattering cross-section significantly decreases.
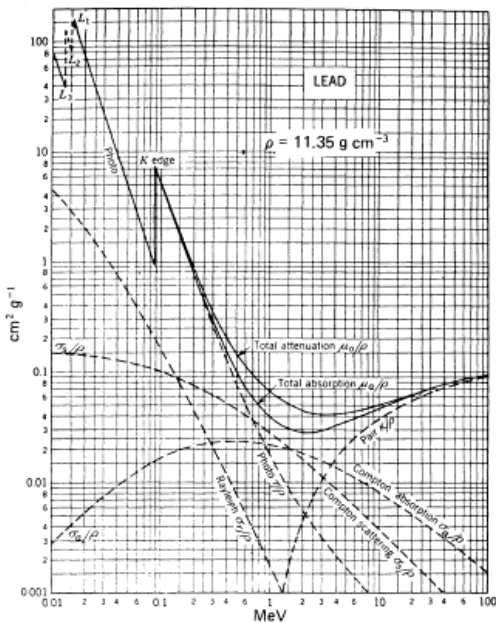


The pair production scattering cross-section close to the threshold is further decreased because to the large recoil energy of the target electron. Indeed, an incident photon deposits its energy not only into the newly created electron-positron pair, but also into the kinetic energy of the initially existing electron. This reduces the amount of energy available for the pair. Once the available energy is below $2m_e$, the pair could no longer be created and the process gets suppressed.

Second possibility for the pair production by a photon propagating through matter is via interaction with protons / atomic nuclei. The high-energy photon could directly interact with the Coulomb field of the nucleus, because its wavelength is much shorter than the size of the atom. In this way, the photon interacts separately with electron or the nucleus, rather than with the entire atom. In the case of scattering of photon on the nucleus the recoil energy of the scattered nucleus is much less, because the nucleus is much heavier than both electron and positron. The kinematics of the scattering in this case is such that photon "bounces" from a proton / nucleus (almost) at rest and is converted into an electron-positron pair. Neglecting the recoil of the nucleus altogether, the process could be described as interaction of photon with the Coulomb field of stationary

Figure 2.14: Energy dependence of photon scattering cross-section in lead.

atomic nucleus.

The cross-section of the pair conversion in the Coulomb field was first calculated by Bethe and

Heitler and is known as the Bethe-Heitler cross-section.

$$\sigma_{N\gamma \to Ne^+ e^-} \simeq \frac{28\alpha^3}{9m_e^2} r_e^2 Z(Z+1) \tag{2.144}$$

As expected, it is proportional to $\alpha^3$. It is much smaller than the Thomson cross-section $\sigma_T = (8\pi/3)(\alpha/m_e)^2$ in the case of scattering on protons. However, in the case of scattering in "high-Z" material with the $Z \gtrsim 1/\sqrt{\alpha}$, the $Z^2$ factor could compensate for the suppression of the cross-section by $\alpha$. Thus, in high-Z materials, the pair production process starts to "compete" with Compton scattering already close to the threshold of the pair production. As an example, Fig. 2.14 shows the energy dependence of the photon scattering cross-section in the lead.



Figure 2.15: The principle of $\gamma$-ray detection by pair conversion telescope.

### 2.9.1  Example: pair conversion telescopes.

The dominance of the pair production over the Compton scattering in the energy range above 10 MeV suggests that telescopes for observations in the energy band above 10 MeV should not be the Compton telescopes (see section 2.7.5), but rather "pair conversion" telescopes. This is the basic idea behind the Fermi Space $\gamma$-ray telescope which is now operating in space[1] and the past EGRET telescope which was operational together with COMPTEL on board of Compton Gamma-Ray Observatory satellite.
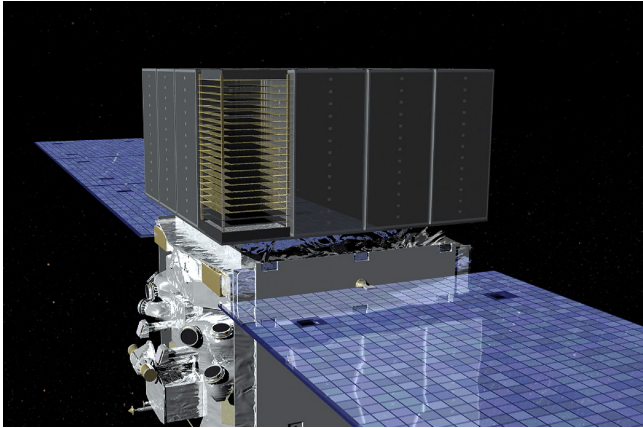


Figure 2.16: Fermi Large Area Telescope: a pair conversion telescope currently operating in orbit. Tracker layers and the calorimeter could be seen in the open part of the telescope box surrounded by an "anti-coincidence" shield rejecting charged cosmic rays which hit the telescope in space.

The principle of operation of a pair conversion telescope is shown in Fig. 2.15. $\gamma$-ray penetrating into the detector volume is converted into electron-positron pair in a high-Z medium. The trajectory of electron and positron is recorded by a tracker, which registers several reference points of passage of the charged particle. In the photon energy range $E_\gamma \gg m_e$ the electron and positron are highly relativistic with the energy $E_{e^+,e^-} \simeq E_\gamma/2 \gg m_e$. The kinematics of the pair production reaction is such that the direction of motions of electron and positron is aligned with the direction of motion of initial $\gamma$-ray to within an angle $\theta \sim E_{e^+,e^-}/m_e \ll 1$. Thus, measuring the direction of motion of the electron and positron, one obtains the information on the arrival direction of the initial $\gamma$-ray.

The sum of energies of electron and positron is equal to the energy of the $\gamma$-ray. Measuring the energies of electron and positron with the help of a calorimeter one finds the energy of the $\gamma$-ray.

Several pair conversion telescopes are currently operating in orbit: Fermi Large Area Telescope (LAT) and AGILE. Fig. 2.16 shows an image of the Fermi/LAT telescope, with the tracker layer clearly seen in the cross-section. Below the tracker layers one could see the thick plate of the calorimeter. The overall dimensions of the telescope are about 1 m $\times$ 1 m. It could detect photons with energies up to $\sim 1$ TeV. Detection of photons of higher energies is limited by two factors. First, high-energy
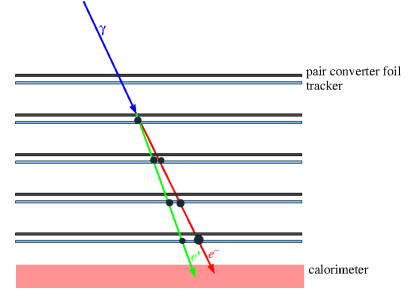
---

[1]http://fermi.gsfc.nasa.gov/ssc/

particle showers developing in the calorimeter start to "leak" from the bottom, so that the shower is not entirely contained in the calorimeter. In this case the calorimeter provides only the measurement of the part of the initial photon energy dissipated in the calorimeter, and not the real shower photon energy.

Another problem is that at TeV energies the flux of photons from astronomical sources becomes very low. To judge how low could be the flux, it is useful to consider Crab nebula, which is one of the brightest $\gamma$-ray sources on the sky. Fig. 2.7 shows that the flux of the source in the TeV range is $\epsilon F_{\epsilon,Crab} \simeq 3 \times 10^{-11}$ erg/cm$^2$ s. Each TeV $\gamma$-ray carries about 1 erg of energy, so that the flux is $F_{\epsilon,Crab} \simeq 3 \times 10^{-11}$ photons/(cm$^2$ s). A telescope with collection area 1 m $\times$ 1 m$= 10^4$ cm$^2$ counts the source photons at the rate $\mathcal{R} \sim 3 \times 10^{-7}$ s which corresponds to approximately one photon per month. Several years of observations are needed to collect the signal containing tens of photons, which is needed for a sensible spectral analysis.

## 2.10  Gamma-gamma pair production.

A quick look at the diagrams shown in Fig. 2.13 gives an idea for another possible type of pair production process, which occurs in $\alpha^2$, rather than $\alpha^3$ order of perturbation theory and, therefore, has a larger cross-section. Indeed, looking at the diagram of Compton scattering, one sees that it describes an interaction which involves two photons and two electrons / positrons. Up to now we have considered the collisions between electrons and photons, with one incoming and one outgoing electron / photon.

The same diagram appears in the calculations of scattering amplitudes of two other processes. The collisions of electrons and positrons might result in disappearance of both particles and appearance of two photons. The process is called annihilation. In this case the diagram has the form shown on the left in Fig. 2.28. Alternatively, in an inverse process, collision of two photons might result in production of an electron positron pair. Counting the vertexes of the diagram we find that these processes occur in the sam order of perturbation theory in $\alpha$, so their cross-sections are comparable to the Thomson cross-section.
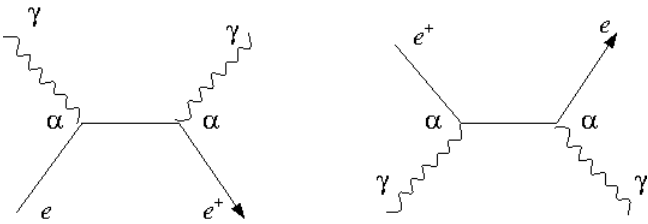


Figure 2.17: Feynman diagrams for annihilation (left) and production of pairs (right).

Pair production on photon-photon collisions is possible only if the center-of-mass energy is higher than two times the rest energy of electron. The energy threshold of the reaction could be found from the four-momentum conservation law. We introduce the notations $\underline{P}_{\gamma 1,2} = (\epsilon_{1,2}, \vec{p}_{1,2})$ for the four-momenta of the two incoming photons in the lab frame and $\underline{\tilde{P}}_{\gamma 1,2} = (\tilde{\epsilon}, \pm \tilde{p})$ for their momenta in the center-of-mass frame. We calculate the four-scalar

$$\underline{P}_{\gamma 1} \underline{P}_{\gamma 2} = \epsilon_1 \epsilon_2 (1 - \cos\theta) = 2\tilde{\epsilon}^2 \tag{2.145}$$

in the lab frame and in the centre of mass frame ($\theta$ is the angle between the directions of the two photons). The outcome of the collision in the venter-of-mass frame are electron and positron at rest. The product of their four momenta is just $2m_e^2$. Equating this to $\underline{P}_{\gamma 1} \underline{P}_{\gamma 2}$ we find that the pair production reaction is possible if

$$\epsilon_{\gamma 1} \epsilon_{\gamma 2} > \frac{2m_e}{(1 - \cos\theta)} \geq m_e^2 \tag{2.146}$$

A typical example of gamma-gamma pair production in the astrophysical conditions is of a source emitting high-energy $\gamma$-rays which, before escaping from the source have to propgate through a soft

photon background. Taking the $\gamma$-ray energy $E_\gamma$ and the typical soft photon energy $\epsilon$, we find that the source potentially becomes opaque to $\gamma$-rays with energies higher than

$$E_\gamma \simeq 250 \left[\frac{\epsilon}{1 \text{ eV}}\right]^{-1} \text{GeV} \tag{2.147}$$



At the energies higher than the threshold, electron and positron move with typical energies $m_e \gamma \simeq \tilde{\epsilon}$ and velocities

$$v \simeq \sqrt{1 - \frac{m_e^2}{\epsilon_1 \epsilon_2}} \tag{2.148}$$

(we take a typical collision angle of 90 degrees, assuming that $\gamma$-rays propagate through isotropic soft photon background). Quantum mechanical calculation gives the expression for the cross-section of the process

$$\sigma_{\gamma\gamma}(v) = \frac{\pi r_e^2}{2}(1 - v^2)\left[2v(v^2 - 2) + (3 - v^4)\ln\left(\frac{1 + v}{1 - v}\right)\right] \tag{2.149}$$

It is useful to compare this cross-section with the cross-section of Compton scattering. Close to the threshold, in the limit $v \to 0$, we find

$$\sigma_{\gamma\gamma} \simeq \pi r_e^2 v \tag{2.150}$$

It reaches $\simeq \pi r_e^2 \simeq \frac{3}{8}\sigma_T \simeq 1.5 \times 10^{-25}$ cm$^2$ at the maximum. At large $v \to 1$, the limit is

$$\sigma_{\gamma\gamma} \simeq \frac{\pi r_e^2 m_e^2}{E_\gamma \epsilon} \ln\left(\frac{E_\gamma \epsilon}{m_e^2}\right) \tag{2.151}$$

i.e. it decreases as $E \ln E$, similarly to the Compton cross-section in Klein-Nishina regime.

A comparison of the energy dependences of the cross-sections of inverse Compton scattering, $\gamma\gamma$ pair production and triplet production is shown in Fig. 2.18.

### 2.10.1 Example: pair production opacity of high-energy sources and of the Universe

The relation between the cross-sections of Compton scattering and pair production has an important implication for the physics of high-energy sources. We remember that many sources (including all the stars) are opaque with respect to the Compton scattering (i.e. the mean free path of photons $\lambda = (\sigma_T n_e)^{-1}$ is much shorter than the size of the source $R$ and the optical depth $\tau = R/\lambda \gg 1$.

This means automatically that the same sources are opaque also to $\gamma$-rays with energies in excess of the pair production threshold (2.147). Indeed, the cross-section of the pair production $\sigma_{\gamma\gamma} \sim 0.1\sigma_T$.

The most famous example of a pair production thick source is given by the Gamma-Ray Bursts (GRB). These are $\gamma$-ray sources which occur for short
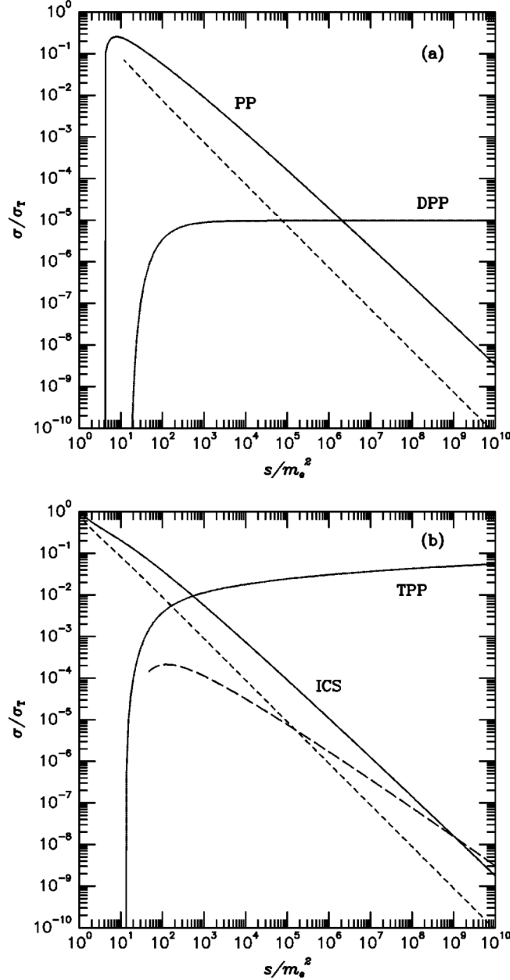
Figure 2.18: Comparison of the cross-sections of inverse Compton scattering (ICS), triplet production (TPP) and $\gamma\gamma$ pair production (PP) as functions of the square of the centre-of-mass energy $s$. Also shown in the cross-section of double pair production (DPP). Solid lines show the cross-sections, dashed lines show cross-sections times the elasticity (average fractional energy loss of electron in single collision). From Ref. [17].

periods of time ($0.1 - 10^3$ s at the moment of supernova explosions). The luminosity of the sources reaches $L_\gamma \simeq 10^{50}$ erg/s, in the soft $\gamma$-ray band $E_\gamma \simeq 1$ MeV. The relation of the source to the star with gravitationally collapsing core suggests an estimate of the source size $R \sim 10^6$ cm, of the order of the gravitational radius of the star $R_g = G_N(10M_\odot) \simeq 10^6$ cm. If we calculate the optical depth of the source with respect to the pair production by the MeV $\gamma$-rays on themselves ($\epsilon \sim E_\gamma \sim 1$ MeV), we find

$$\tau = \frac{R}{\lambda_{\gamma\gamma}} \simeq \frac{L_\gamma \sigma_{\gamma\gamma}}{4\pi R \epsilon} \tag{2.152}$$

we would find a value in the range of $10^{14}$. This implies that the MeV $\gamma$-rays should not escape from the source at all. We will see later on in the course (when considering the GRB phenomenon) how this difficulty in source modelling is overcome. This pair production opacity problem is encountered in a milder form in a number of other high-energy source types, like e.g. active Galactic Nuclei.



Figure 2.19: Comparison of the energy-dependent mean free path of $\gamma$-rays with the distances to the known TeV $\gamma$-ray sources.

Another common example of a source opaque w.r.t. the pair production is the Universe itself. Indeed, the Universe is filled with radiation fields (the CMB, the interstellar radiation field in our Galaxy, the Extragalactic Background Light, which is the infrared radiation field collectively produced by all the galaxies in the course of cosmological evolution). The energy of CMB photons is $\epsilon \simeq 10^{-3}$ eV. This means that $\gamma$-rays with energies higher than $E_\gamma \simeq 0.3$ PeV (see eq. (2.147)) could produce pairs in interactions with CMB photons. The density of the CMB photons is $n_{CMB} \simeq 400$ cm$^{-3}$. The mean free path of the $\gamma$-ray s w.r.t. the pair production is, therefore,

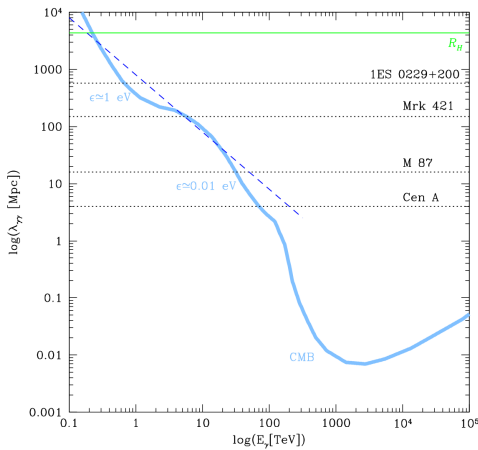$$\lambda_{\gamma\gamma} = \frac{1}{\sigma_{\gamma\gamma} n_{CMB}} \simeq 8 \text{ kpc} \tag{2.153}$$

Thus, PeV $\gamma$-rays are even not able to escape from the host galaxy of the source (typical galaxy sizes are 10-100 kpc).

Otherwise, lower energy TeV $\gamma$-rays could efficiently produce pairs in interactions with the EBL photons of the energies $\epsilon \simeq 1$ eV. The density of the EBL is much lower and the mean free path of photons w.r.t. this process is respectively larger. Still it is shorter than the typical distance to the extragalactic sources of TeV $\gamma$-rays. Comparison of the $\gamma$-ray mean free path with the distances to the known TeV sources is shown in Fig. 2.19.
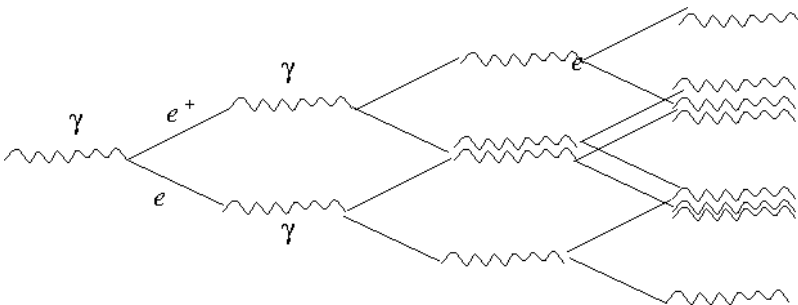
### 2.10.2   Electromagnetic cascades



Figure 2.20: Model of electromagnetic cascade.

The pair production converts high-energy $\gamma$-rays into electrons and positrons of comparable energies. The inverse Compton scattering process re-generates the high-energy $\gamma$-rays by transferring the energy of electrons / positrons to the low-energy photons. In this way, a cyclical process of "bouncing" of the energy between

electrons / positrons and γ-rays could take place. This process also leads to multiplication of the number of high-energy particles, because each pair production event generates two high-energy particles (electron and positron) of of one high-energy γ-ray.

This process is called electromagnetic "cascade". It is important in the context of several astrophysical situations, in particular, in the interiors of some high-energy sources.

A simple phenomenological description of the cascade is shown in Fig. 2.20. The mean free path of photons w.r.t. the pair production is comparable to that of electron / positron w.r.t. the inverse Compton scattering (in Klein-Nishina regime). After propagating approximately one mean free path distance, the γ-ray of energy $E_0$ disappears and transfers energy to electron and positron in roughly equal proportions, so that the energies of both particles are $E_{e,1} \sim E_0/2$. Inverse Compton scattering in the Klein-Nishina regime converts most of the electron /positron energy back into γ-ray energy, so that the energy of the "first generation" γ-rays are $E_{\gamma,1} \simeq E_0/2$. The process of division of energy between new particles repeats in the "second generation of the cascade. After $n$ generations, the typical energy of the cascade particles is

$$E_{e,n} \simeq E_{\gamma,n} \simeq \frac{E_0}{2^n} \tag{2.154}$$

The number of particles in the cascade is

$$N_n \simeq 2^n \tag{2.155}$$

The process of energy division repeats until the energies of particles decrease below the pair production threshold. If the highers energy γ-rays are continuously injected in the source, an equilibrium distribution forms with time. In this equilibrium distribution the spectrum of cascade particles is

$$N(E) \sim (E/E_0)^{-1} \tag{2.156}$$

which implies a $dN/dE \sim E^{-2}$ type (again!) differential spectrum.

## 2.11   Bremsstrahlung

Up to now we have concentrated on the radiative losses of electrons due to the interactions with magnetic field (synchrotron) and radiation fields (inverse Compton). High-energy electrons also suffer from energy losses when they propagate through matter and interact with the electrostatic Coulomb field of atomic nuclei. There are two energy loss channels: radiative one, called Bremsstrahlung, and non-radiative one, called ionisation loss.

The radiative energy loss is related to the accelerated motion of electron which is deviated by the Coulomb field of an atomic nucleus. The power of radiation is given by the conventional Larmor formula $d\mathcal{E}/dt = (2/3)|\ddot{p}|^2$, where $\vec{p} = e\vec{r}$ is the dipole moment. If we consider spectral decomposition of the power, we use the formula

$$\frac{d\mathcal{E}}{d\omega} = \frac{8\pi}{3}\omega^4|\hat{p}(\omega)|^2 \tag{2.157}$$

where $\hat{p}(\omega)$ is the Fourier transform of the dipole moment.

Considering the geometry and physics of scattering of electron in the Coulomb field of the nucleus (see Fig. 2.21), we know that the scattering takes place on the time scale $\tau \simeq b/v$ where $b$ is the "shooting parameter" and $v$ is velocity of the particle. This implies that the spectrum of Bremsstrahlung extends up to the frequency $\omega \sim 2\pi/\tau \simeq 2\pi v/b$. Numerically,

$$\omega^2\hat{\vec{p}}(\omega) = \frac{e}{2\pi}\int_{-\infty}^{\infty}\ddot{\vec{r}}e^{i\omega t}dt = \frac{e}{2\pi}\int_{-\infty}^{\infty}\dot{\vec{v}}e^{i\omega t}dt \tag{2.158}$$

The expression under the integral is strongly oscillating in the limit $\omega \to \infty$, so that the integral is indeed approximately zero. In the limit $\omega \ll 2\pi v/b$, the exponential term in the integral stays roughly

constant on the time scale $t \sim \tau$, so that we could in the first approximation substitute this term with 1. This gives

$$\omega^2 \hat{\vec{p}}(\omega) \simeq \begin{cases} \frac{e}{2\pi} \int \dot{v} dt = (e/2\pi)\Delta v, & \omega \ll 2\pi v/b; \\ 0, & \omega \gg 2\pi v/b. \end{cases} \tag{2.159}$$

where $\Delta v$ is the overall change of velocity in the scattering event.

This overall velocity change could be found from the dynamics of scattering. The second law of Newton reads

$$m_e \dot{\vec{v}} = -e\vec{E} \tag{2.160}$$

where $\vec{E}$ is the electric field of the atomic nucleus with the charge $Ze$, $\vec{E} = Ze^2\vec{r}/r^3$. In the first approximation, we could assume that electron moves along a straight line before and after the scattering event at the moment $t = 0$, so that the distance between the electron and the nucleus changes in time as

$$r(t) = \sqrt{b^2 + v^2t^2} \tag{2.161}$$

Besides, we could consider only the acceleration component normal to the electron velocity, taking into account only one component of the electric field. This gives for $\Delta v$

$$\Delta v = \int_{-\infty}^{\infty} \dot{v} dt = \frac{2Ze^2}{m_e} \int_0^{\infty} \frac{bdt}{(b^2 + v^2t^2)^{3/2}} = \frac{Ze^2}{m_ebv} \tag{2.162}$$

Substituting the above expressions into the expression for the radiated power we find

$$\frac{d\mathcal{E}}{d\omega} = \begin{cases} \frac{2e^2}{3\pi} \frac{4Z^2e^4}{m_e^2b^2v^2}, & \omega \ll 2\pi v/b; \\ 0, & \omega \gg 2\pi v/b \end{cases} \tag{2.163}$$

We notice that the power of radiation scales with the square of the charge of the nucleus. The power is higher for close encounters (smaller $b$) and slow electrons (smaller $v$).
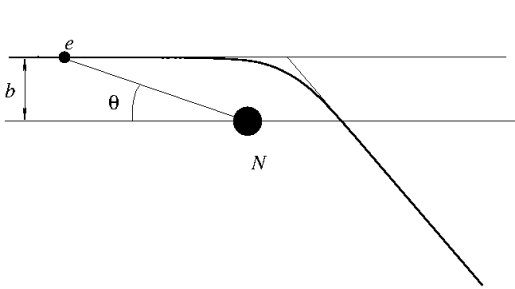


Figure 2.21: Geometry of scattering of electron on an atomic nucleus.

A typical situation is when electron propagates through a medium. The rate of encounters with different $b$ is determined by the density of the medium. The total energy of Bremsstrahlung emission after the path length $H = vt$ is then found as an integral over $b$

$$\frac{d\mathcal{E}_{tot}}{d\omega} = \int \frac{d\mathcal{E}}{d\omega} 2\pi nHb \, db \tag{2.164}$$

wheree $n$ is the density of the medium. The explicit expression is

$$\frac{d\mathcal{E}_{tot}}{d\omega \, dt} = \frac{16}{3} \frac{Z^2e^6n}{m_e^2v} \int \frac{db}{b} = \frac{16}{3} \frac{Z^2e^6n}{m_e^2v} \ln\left(\frac{b_{max}}{b_{min}}\right) = \frac{16\pi Z^2e^6n}{3\sqrt{3}m_e^2v} g_{ff}(v,\omega) \tag{2.165}$$

where $b_{min}, b_{max}$ are the minimal and maximal values of the shooting parameter, which are rather difficult to estimate. A way around this difficulty is to introduce the so-called Gantt factor

$$g_{ff}(v,\omega) = \frac{\sqrt{3}}{\pi} \ln\left(\frac{b_{max}}{b_{min}}\right) \tag{2.166}$$

This phenomenological factor $g_{ff} \sim 1$ is tabulated for different materials. The $ff$ subscript is for "free-free" emission, another name for Bremsstrahlung in English.

Qualitatively, the maximal and minimal values of the shooting parameter are readily understood. For very slow particles, the minimal possible value is determined by the quantum mechanical extent of the electron wave function, which is estimated form the uncertainty relation

$$\Delta p \Delta x \simeq m_e \Delta v b_{min} \sim 1 \tag{2.167}$$

which gives $b_{min} \sim (m_e v)^{-1}$, about the deBroglie wavelength. Otherwise, the distance of closest approach of the fast particles is estimated from the relation

$$\frac{m_e v^2}{2} \sim \frac{Ze^2}{b_{min}} \tag{2.168}$$

which gives $b_{min} \sim Ze^2/m_e v^2$. The real value of $b_{min}$ is the smaller of the two estimates.

The maximal value $b_{max}$ at which the Bremsstrahlung emission is contributing to the power at a frequency $\omega$ is estimated from the relation $\omega < 2\pi v/b_{max}$, which gives an estimate $b_{max} \sim 2\pi v/\omega$. Of course, the maximal value of $b$ could not be smaller than the minimal, which imposes an evident restriction on $\omega$

$$\omega < m v_e^2 \sim E_e \tag{2.169}$$

i.e. the energy of the Bremsstrahlung photons could not exceed the energy of the parent electron.

Inspecting the Eq. 2.165 we notice that the power of Bremsstrahlng emission scales with the energy of electron as

$$\frac{d\mathcal{E}}{dt} \simeq \omega \frac{d\mathcal{E}}{d\omega dt} \sim v \sim E_e^{1/2} \tag{2.170}$$

in the case of non-relativistic electrons considered so far.



Figure 2.22: X-ray image of Coma galaxy cluster

The expression for the Bremsstrahlung spectrum in the relativistic case is similar to the non-relativistic expression:

$$\frac{d\mathcal{E}}{d\omega dt} \simeq \frac{Z^2 e^6 n}{m_e^2 v} \ln\left(\frac{192v}{Z^{1/3}}\right) \tag{2.171}$$
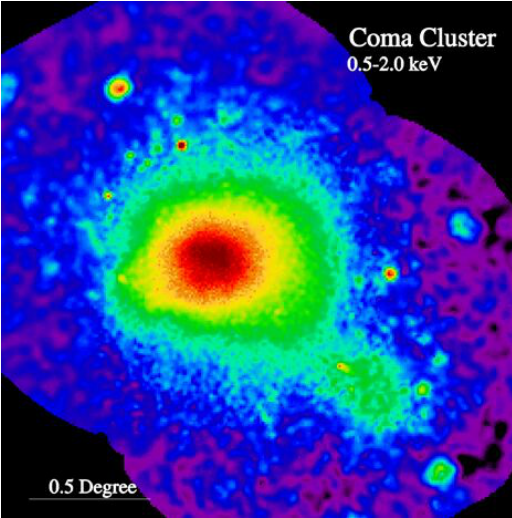
However, the same formula implies a different scaling of the Bremsstrahlung power with the election energy:

$$\frac{d\mathcal{E}}{dt} \simeq \omega \frac{d\mathcal{E}}{d\omega dt} \simeq \frac{Z^2 e^6 n E_e}{m_e^2} \sim E_e \tag{2.172}$$

This implies that the Bremsstrahlung cooling time

$$t_{brems} = \frac{E_e}{dE_e/dt} \simeq \frac{m_e^2}{Z^2 e^6 n} = \frac{1}{\sigma_{brems} n} \tag{2.173}$$

is roughly energy independent for relativistic particles. We have introduced in the last equation the cross-section $\sigma_{brems} \simeq Z^2 e^6/m_e^2$ One could notice that this cross-section is

$$\sigma_{brems} \sim 10^{-2} Z^2 \sigma_T \tag{2.174}$$

similarly to the cross-section of Bethe-Heitler pair production.

### 2.11.1 Example: thermal Bremsstrahlung X-rays from galaxy clusters

The Bremsstrahlung emission is responsible for the X-ray flux from galaxy clusters. Gas which falls in the gravitational potential well of the clusters with mass $M \sim 10^{15} M_\odot$ heats liberates its gravitational potnetial energy which is converted in the energy of the random motions of particles or, in other words into heat. The temperature of the gas could be estimated from the virial theorem

$$T \sim \frac{mv^2}{2} \sim \frac{GMm_p}{R} \sim 10 \ keV \left[ \frac{M}{10^{15}M_\odot} \right] \left[ \frac{R}{1 \ \text{Mpc}} \right]^{-1} \tag{2.175}$$

Gas heated to this temperature emits Bremsstrahlung photons with energies comparable to the energies of electrons in the gas, see Fig. 2.22 for an example of X-ray Bremmstrahlung emission from Coma galaxy cluster. .

Density of the gas in the cluster is $n \sim 0.05 M/R^3 \sim 10^{-3}$ cm$^{-3}$. The Bremsstrahlung cooling time

$$\frac{E}{dE/dt} \simeq \frac{3m_e^{3/2}T^{1/2}}{16\pi Z^2 e^6 n} \sim 10^{10} \left[ \frac{n}{10^{-3} \ \text{cm}^{-3}} \right]^{-1} \left[ \frac{T}{10 \ \text{keV}} \right]^{1/2} \ \text{yr} \tag{2.176}$$

This time is comparable to the age of the Universe, so that the hot gas residing in the clusters is about to cool down at the present epoch of evolution of the Universe. Gas cooling is expected to produce a "cooling flow" with decreasing temperature and increasing density in the center of the clusters. The increase of the density and decrease of temperature speed up the coouling so that the cold gas should quickly accumulate in the cluster core.

This cooling flow process is most of the time counteracted by the activity of the centerl galaxy of the cluster which produces relativistic outflows displacing the cooling flow and heating the intracluster medium.

## 2.12 Ionisation losses

The energy loss of electron scattering on an atomic nucleus is not limited to the radiative Bremsstrahlung loss. Another energy loss channel is the kinetic energy of nucleus recoil. We could estimate the momentum which the nucleus gets in a single scattering event via a calculation similar to that done for the estimation of electrons $\Delta v$ in the previous section. We approximate the motion of electron as a straight line before and after the scattering event at the moment $t = 0$ and write the expression for the electrostatic force acting on the nucleus

$$F_\perp = \frac{Ze^2 b}{r^3} \tag{2.177}$$

(we take into account only the component normal to the electron velocity). The work done by the force is the change of momentum of the nucleus

$$\Delta p = 2 \int_0^\infty F_\perp dt = \int F_\perp \frac{bd\theta}{\sin^2 \theta} = \frac{Ze^2}{bv} \int_0^\pi \sin \theta \ d\theta = \frac{2Ze^2}{bv} \tag{2.178}$$

using the notation for the angle $\theta$ introduced in Fig. 2.21.

The momentum conservation law tells that the momentum gained by the nucleus is equal to the momentum lost by the electron. The electron energy loss associated to the exchange of momentum between the electron and the nucleus is

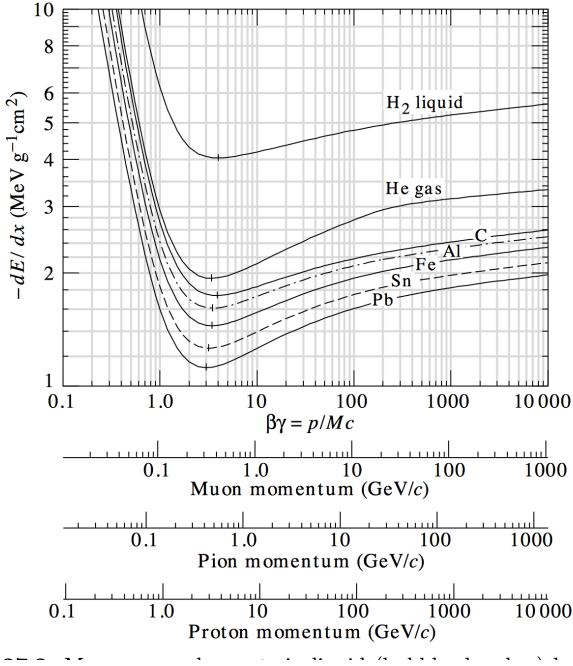$$\Delta \mathcal{E}_e = \frac{\Delta p^2}{2m_e} = \frac{2Z^2 e^4}{m_e b^2 v^2} \tag{2.179}$$

Figure 2.23: The rate of ionisation loss as a function of momentum of high-energy particle

Electron propagating through a medium interacts with many nuclei at different shooting parameters $b$. The overall energy transferred to the nuclei per path length $dx$ is

$$\frac{d\mathcal{E}_e}{dx} = \int 2\pi nb \; db \frac{2Z^2 e^4}{m_e b^2 v^2} = \frac{4\pi Z^2 e^4 n}{m_e v^2} \ln \left( \frac{b_{max}}{b_{min}} \right) \quad (2.180)$$

and expression similar to that for the Bremsstrahlung energy loss. A more general relativistic expression for the ionisation loss is given by the Bethe-Bloch formula

$$\frac{d\mathcal{E}_e}{dx} = \frac{4\pi Z^2 e^4 n}{m_e v^2} \left[ \ln \left( \frac{2\gamma^2 m_e v^2}{I} \right) - v^2 \right] \quad (2.181)$$

where $I$ is the ionisation energy of the atoms composing the medium. Taking a medium with the density water, $n \simeq 10^{24}$ cm$^{-3}$, we could estimate the energy loss as

$$\frac{d\mathcal{E}_e}{dx} \simeq (several) \text{ MeV/cm} \quad (2.182)$$

for a mildly relativistic electron ($v \sim 1, \quad \gamma \sim 1$). The energy dependence of ionisation loss has a pronounced minimum at $v\gamma \simeq 3$, see Fig. 2.23. Particles of this energy are called "minimum ionising particles" in particle physics.

It is interesting to note that the ionisation loss calculation which we've done for the electron "pulling" the heavy atomic nuclei could be re-used to calculate the energy loss of a heavy particle (e.g. an atomic nucleus, but could also be muon, pion etc.) propagating through a medium filled with electrons. In this case, trajectory of the heavy particle is almost not deviated, but electrons in the medium gain momentum when the particle passes next to them. The momentum gain of each electron is still given by Eq. (2.178) and the overall energy loss of the heavy particle is still given by Eq. (2.180). Thus, it appears that any particle propagating through the medium experiences approximately the same energy loss at a given velocity. This is illustrated in Fig. 2.23 where the X axis shows not only the momenta of different particles.

A proton of the energy 1 GeV looses $\simeq 2$ MeV/cm on the Coulomb / ionisation loss while propagating through the medium, i.e. the same amount of energy as an electron of the energy 0.5 MeV. Because of this fact, heavy particles have much higher "penetrating power". A proton of the energy 1 GeV would loose a significant fraction of its energy on ionisation after $\simeq 1$ GeV/(2 MeV/cm) $\simeq 500$ cm, while electron would loose all its energy within $\simeq 0.5$ MeV/(2 MeV/cm) $\simeq 0.25$ cm distance.

The ionisation energy loss rate of relativistic particles grows only logarithmically with energy. This means that the ionisation loss time

$$t_{ion} = \frac{\mathcal{E}_e}{d\mathcal{E}_e/dt} \sim \frac{E_e}{\ln(E_e)} \quad (2.183)$$

becomes longer with the increasing energy. Comparing the ionisation and Bremsstrahlung energy loss times we find

$$\frac{t_{ion}}{t_{brems}} \simeq \frac{Z^2 e^6 n E_e}{m_e^2 v} \frac{m_e v^2}{Z^2 e^4 n} \sim \frac{e^2 E_e}{m_e} \quad (2.184)$$

we find that as soon as the gamma-factor of electron $E_e/m_e$ reaches $1/e^2 \sim 100$, the Bremsstrahlung energy loss starts to dominate over the ionisation energy loss.

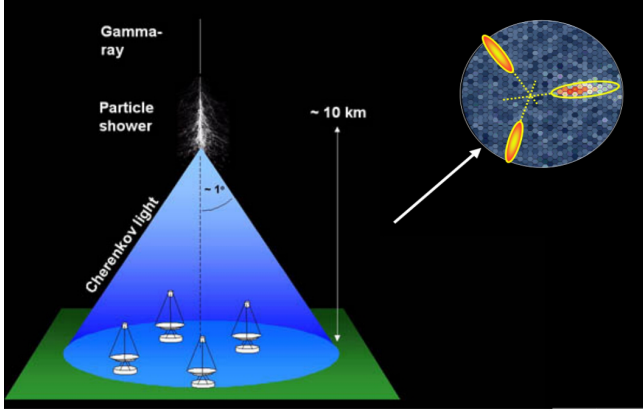### 2.12.1 Example: extensive air showers in the atmosphere.



Figure 2.24: Principle of observation of EAS initiated by $\gamma$-rays and cosmic rays by the imaging atmospheric Cherenkov telescopes.

We have considered in Section 2.10.2 the phenomenon of electromagnetic cascade taking place during propagation of $\gamma$-rays and electrons through a photon gas. A similar cascade phenomenon also accompanies propagation of high-energy particles through a medium.

One particularly interesting example is that of particle cascades in the atmosphere, called "Extensive Air Showers". A high-energy $\gamma$-ray (or any other high-energy particle hitting the atmosphere) will interact with atoms (electrons, nucleons). The main interaction channel for the $\gamma$-rays with energies above MeV is the Bethe-Heitler pair production. The cross-section of the pair production is $\sigma_{BH} \sim Z^2 e^6 / m_e^2$ and the mean free path of the $\gamma$-ray through the air is

$$\lambda_\gamma = \frac{1}{\sigma_{BH} n_{air}} \simeq 10^5 \text{ cm} \qquad (2.185)$$

, ($n_{air} \simeq 10^{21}$ cm$^{-3}$ is the density of the atmosphere). It is much shorter than the scale height of the atmosphere, $H_{air} \sim 10$ km. Thus, high-energy photons do not reach the ground level and are, instead, converted into electron-positron pairs.

Electrons and positrons with energies above $\sim 100$ MeV loose energy mostly via Bremsstrahlung emission. The energy of the Bremmstrahlung photons reaches that of electrons. The cross-section of the Bremsstrahlung is comparable to that of the pair production. Thus, after one more $\lambda_\gamma$ distance all the energy of electrons and positrons is converted back into $\gamma$-rays, although with energies lower than that of the initial $\gamma$-ray. The whole process of conversion of energy between $\gamma$-rays and electrons / positrons repeats again. In this way an electromagnetic cascade similar to that described in Section 2.10.2 develops until the energies of electrons and photons reach the critical energy at which the Bremsstrahlung energy loss becomes sub-dominant compared to the ionisation energy loss ($E_{e,crtit} \simeq 100$ MeV). As soon as the energy drops below the critical energy, particle number multiplication in the cascade stops because most of the energy is lost in a non-radiative way on the ionisation.

The maximal number of particles in the EAS could be estimated as $N_{max} \simeq E_0/E_{crit}$ where $E_0$ is the energy of the primary particle which initiated the cascade. This maximum is reached after $n \simeq \ln(E_0/E_{crit})$ generations of cascade at the atmospheric depth $n\lambda_\gamma$.

The EAS initiated by high-energy particles penetrating into the atmosphere could be observed using several complementary techniques. One possibility is to observe blue-violet Cherenkov emission produced by particles moving with the speed faster than the speed of light in the atmosphere. This emission is concentrated in a narrow cone with an opening angle $\alpha_{Ch} = \arccos(1/n_{air}) \simeq 1°$, where $n_{air}$ is the refraction coefficient of the air. The overall intensity of emission from a shower is proportional to the number of charged particles in the EAS and, therefore, to the energy of the primary particle. Imaging the blue-UV trace of the EAS in the atmosphere one could measure the arrival direction of the primary particle.

This technique is used for the observations of $\gamma$-rays with energies in the 0.1-10 TeV range using Imaging Atmospheric Cherenkov Telescopes (IACT), see Fig. 2.24. These telescopes are large optical reflectors with mirror areas in the 100 m$^2$ range, to collect sufficiently strong signal from the EAS. The focal plane of the reflectors is equipped with cameras taking images of the sky on the (tens of) nano-second time scale, characteristic for the duration of of Cherenkov signal. IACTs are conventionally arranged in arrays of several units, to allow stereo-vision technique for the reconstruction of

3d geometry of the EAS in the atmosphere. An example of a telescope belonging to an IACT array MAGIC is shown in Fig. 1.7.
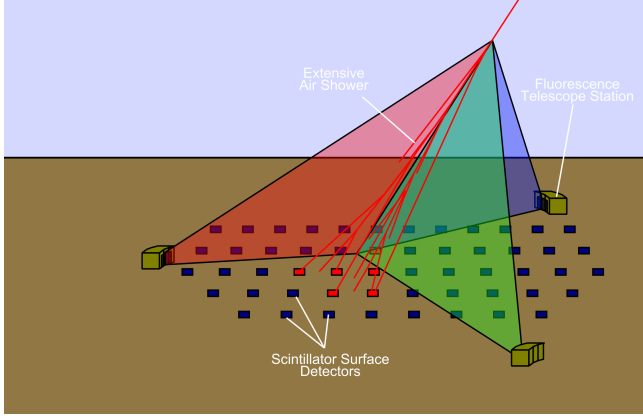


Figure 2.25: Principle of observation of EAS by the air fluorescence telescopes and surface Air Shower Arrays.

Another possibility for the observations of the EAS is to detect the fluorescence light produced by the de-excitations of the air molecules excited by the EAS. If the medium through which the high-energy particles propagate consists of atoms and molecules, transfer of energy to the electrons and nuclei of the medium finally leads to the excitation of the atoms and molecules containing these electrons and nuclei. De-excitation of the $N_2$ molecules in the air produces blue fluorescence light which could be observed during the period of EAS development in the atmosphere (the typical time span is $H/c \simeq 30$ $\mu$s). The fluorescence signal is produced along the EAS track in the atmosphere. Using the stereo vision technique, one could reconstruct the arrival diration of the primary high-energy particles from the track signal in different "air fluorescence" telescopes, as it is shown in Fig. 2.25. This observational principle is realised in experiments studying the highest energy cosmic rays (particle energies above $\sim 10^{18}$ eV), such as Pierre Auger Observatory and Telescope Array experiments.

Still another possible way of detection the EAS is via deployment of a large grid of particle detectors on the ground, as it is shown in Fig. 2.25. The EAS particles reaching the ground level produce signal in many detectors simultaneously. Measurement of the delays between the arrival times of the EAS signal in different detectors provides a possibility to measure the arrival direction of the EAS. Measurement of the overall strength of the signal provides an estimate of the energy of the primary particle which has initiated the EAS. Numerous EAS surface arrays are deployed around the world for observations of cosmic rays and $\gamma$-rays with energies above $\sim 1$ TeV up to the ultra-high-energy cosmic ray energy range, $\sim 10^{20}$ eV.

## 2.13   Interactions of high-energy protons

Up to now we have (almost) neglected radiative energy losses of protons and atomic nuclei. The reason for this is that in most of the cases the energy losses scale inversely proportional to a power of the particle mass and, as a consequence, they are much smaller for heavy protons than for the light electrons. We have seen this on example of the synchrotron radiation.

However, there are several cases when the radiative energy losses of high-energy protons and atomic nuclei are important in the astrophysical context. In this section we will go through the radiative losses of protons and nuclei.

### 2.13.1   Synchrotron, Compton etc losses for protons

In general, all the "classical radiative energy losses which we considered so far are different manifestations of dipole radiation of accelerated particles. The Larmor formula for the dipole radiation power is

$$P = \frac{2e^2}{3}\gamma^4 a_\perp^2 \tag{2.186}$$

From this expression it is clear that particles accelerated in a similar way emit comparable power if their gamma factors are comparable. Thus, if we compare the energy loss of electrons and protons of the same energy, the energy loss of protons will be suppressed, because their gamma factor is by a factor of $m_p/m_e \sim 2 \times 10^3$ lower.

This applies for all the main classical radiative losses, including curvature, synchrotron, inverse Compton and Bremsstrahlung radiation. Nevertheless, the energy losses of extremely energetic protons with large gamma factors could be important in some astrophysical conditions as e.g. discussed in section 2.6.2.

### 2.13.2   Pair production

Energy losses for protons are more important for the quantum processes of production of new particles. The first example is given by the process of pair production in interactions of high-energy protons with low energy photon background. This process is essentially the same as the Bethe-Heitler pair production by $\gamma$-rays propagating through a medium.

Consider an interaction of proton with the four-momentum $\underline{P}_p = (m_p\gamma, m_p\gamma\vec{v})$ with a low energy photon with four-momentum $\underline{P}_\gamma = (\epsilon, \vec{p})$. Let us make a Lorentz transformation to the frame comoving with the proton. In this frame the four-momentum of proton is $\underline{\tilde{P}}_p = (m_p, 0)$, and photon momentum is $\underline{\tilde{P}}_\gamma = (\tilde{\epsilon}, \tilde{p})$. We take the product

$$m_p\gamma\epsilon(1 - v\cos\theta) = \underline{P}_p\underline{P}_\gamma = \underline{\tilde{P}}_p\underline{\tilde{P}}_\gamma = m_p\tilde{\epsilon} \tag{2.187}$$

where $\theta$ is the collision angle in the lab frame. Neglecting the recoil of the proton in the comoving frame, the condition for the possibility of the pair production is that the energy of photon should be higher than the rest energy of the pair, $\tilde{\epsilon} > 2m_e$. This imposes a restriction

$$E_p\epsilon = \frac{m_p\tilde{\epsilon}}{1 - \cos\theta} > \frac{2m_pm_e}{1 - \cos\theta} > m_pm_e \tag{2.188}$$

for the threshold of the reaction. For example, protons propagating through a gas of photons from the starlight, $\epsilon \sim 1$ start to produce pairs if their energy is higher than

$$E_{p,thr} = \frac{m_pm_e}{\epsilon} \simeq 5 \times 10^{14} \left[\frac{\epsilon}{1 \text{ eV}}\right]^{-1} \text{ eV} \tag{2.189}$$

The cross-section of the pair production process is the Bethe-Heitler cross-section,

$$\sigma_{p\gamma \to pe^+e^-} \simeq \frac{56}{9}\alpha r_e^2 \simeq 4 \times 10^{-27} \text{ cm}^2 \tag{2.190}$$

In spite of the sizeable cross-section, the efficiency of the pair production as proton energy loss in astrophysical conditions is usually very low. This is because of the small "inelasticity" of the process. The proton looses only a small fraction of its energy in each pair production event. Indeed, consider the pair production near the threshold. In the reference system comoving with the proton, both the proton and the newly produced electron and positron are almost at rest. Their energies are $m_p$ and $m_e$, respectively. Transforming to the lab frame, both the proton and the election energy is boosted by the proton gamma factor, to $m_p\gamma$ and $m_e\gamma$, respectively. This means that the electron and positron carry away only a small fraction, $\kappa = 2m_e/m_p \simeq 10^{-3}$ of the proton energy. A significant decrease of the proton energy could happen only after $\sim 10^3$ pair production events.

A reference example of marginally important pair production by protons is given by the effect of interactions of high-energy cosmic ray protons with the CMB photons. The threshold energy for this process is $E_{p,thr} \simeq 10^{18}$ eV. The density of CMB is $n_{CMB} \simeq 400$ ph/cm$^3$. Proton mean free path w.r.t. the pair production is

$$\lambda_{p\gamma \to pe^+e^-} = \frac{1}{\sigma_{p\gamma \to pe^+e^-}n_{CMB}} \simeq 10^{24} \text{ cm} \simeq 0.3 \text{ Mpc} \tag{2.191}$$

The energy loss distance is much larger,

$$l_{p\gamma \to pe^+e^-} = \kappa^{-1}\lambda_{p\gamma \to pe^+e^-} \simeq 300 \text{ Mpc} \tag{2.192}$$

This corresponds to the energy loss time $t = l_{p\gamma \to pe^+e^-} \simeq 1$ Gyr, just an order of magnitude below the age of the Universe.

The pair production on CMB might have a small effect on the spectrum of cosmic rays, by slightly suppressing the flux of cosmic rays of the energy $10^{18}$ eV which interact with CMB most efficiently and transfer part of their energy to the pairs.

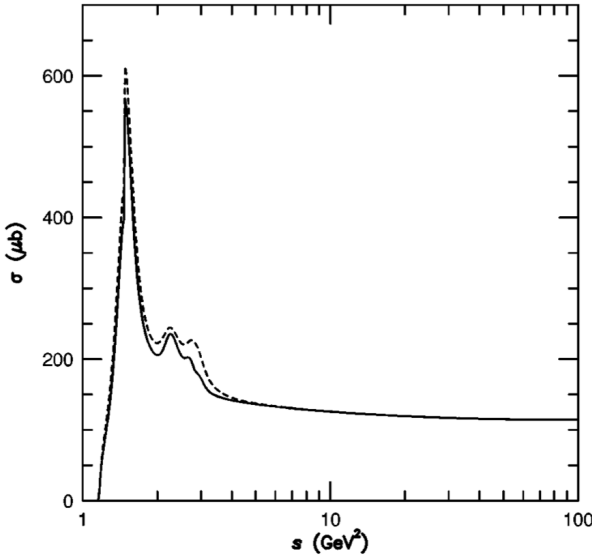### 2.13.3  Pion production and associated electromagnetic emission



A more efficient energy loss of protons is via production of heavier particles, e.g. pions. Pions are two-quark particles with masses in the $m_\pi \simeq 100$ MeV range, i.e. two orders of magnitude higher than electron. Repeating the calculation which led to the estimate inelasticity, we find that in the case of the pion production the inelasticity $\kappa \simeq m_\pi/m_p \simeq 0.1$ is much higher. This means that proton looses a significant fraction of its energy in just several collisions.

The threshold for this reaction could be also found from the kinematics considerations. Introducing, as before, the proton and photon four-momena and transforming to the center-of-mass frame where $\underline{\tilde{P}}_p = (\tilde{E}_P, \vec{\tilde{p}}_p)$ and $\underline{\tilde{P}}_\gamma = (\tilde{\epsilon}, \vec{\tilde{p}}_p)$, we could write an expression for the absolute value of the total four-momentum before and after the reaction $p + \gamma \to p(n) + \pi$. This gives

Figure 2.26: Cross-section of pion production in $p\gamma$ collisions.

$$\left(\underline{P}_p + \underline{P}_\gamma\right)^2 = m_p^2 + 2m_p\gamma\epsilon(1 - v\cos\theta) \tag{2.193}$$

before the reaction (in the lab frame) and

$$\left(\underline{\tilde{P}}_p + \underline{\tilde{P}}_\pi\right)^2 = m_p^2 + 2m_pm_\pi + m_\pi^2 \tag{2.194}$$

after the reaction (the expression is in the center-of mass frame and both proton and pion are at rest after the reaction). Equating the two expressions for the conserved quantity we find the condition for the possibility of the pion production $E_p > E_{p,thr}$,

$$E_{p,thr} = \frac{m_pm_\pi(1 + m_\pi/(2m_p))}{2\epsilon} \simeq 10^{17} \left[\frac{\epsilon}{1 \text{ eV}}\right]^{-1} \text{ eV} \tag{2.195}$$

The cross-section of this process is determined by the physics of strong interactions. Close to the threshold is is as large as $\sigma_{p\gamma} \simeq 6 \times 10^{-28}$ cm and drops to $\simeq 10^{-28}$ cm much above the threshold, see Fig. 2.26.

The inelasticity of the pion production collisions is higher than that of the electron-positron pair production, The fraction of energy lost by proton in each collision is $\kappa \sim 10^{-1}$ rather than $\sim 10^{-3}$.

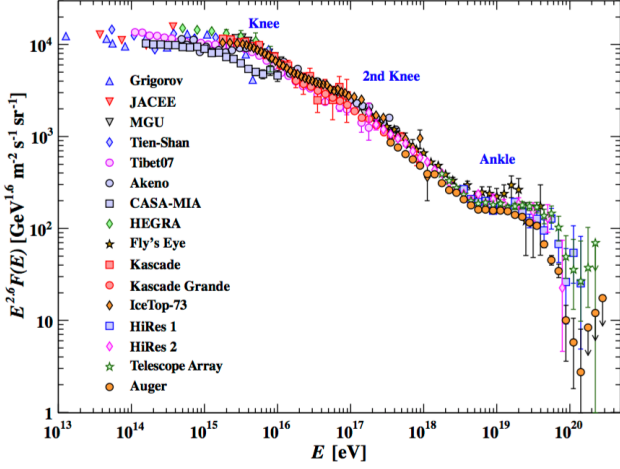**Example: GZK cutoff in the spectrum of cosmic rays**

Figure 2.27: Spectrum of cosmic rays [18].

If we consider again the example of cosmic rays interacting with the CMB photons, we find that the mean free path and the energy loss with respect to the pion production reaction are, respectively, longer and shorter, compared to the pair production

$$\lambda_{p\gamma} = \frac{1}{\sigma_{p\gamma} n_{CMB}} \simeq 1 - 10 \text{ Mpc} \qquad (2.196)$$

and the energy loss distance

$$l_{p\gamma} = \kappa^{-1} \lambda_{p\gamma} \simeq 10 - 100 \text{ Mpc} \qquad (2.197)$$

The pion production loss has, therefore, stronger effect on the cosmic rays spectrum, significantly suppressing the flux of cosmic rays with energies $E_p > E_{p,thr} \simeq 10^{20} \left[\epsilon / 10^{-3} \text{ eV}\right]^{-1}$ eV. This is the domain of Ultra-High-Energy Cosmic Rays (UHECR), the highest energy particles ever detected. The interactions with the CMB suppress the flux of cosmic rays above the threshold of the pair production. This effect is know Greisen-Zatsepin-Kuzmin (GZK) cut-off.

The GZK cut-off is possibly observed in the spectrum of UHECR, see Fig. 2.27. This cut-off is expected to appear as a suppression of the cosmic rays flux at the energies above $10^{20}$ eV. Such suppression is clearly seen in the data as a deviation from the powerlaw extrapolation of the spectrum from the energy band $\sim 10^{19}$ eV.

There is, however, no unambiguous interpretation of the observed suppression of the flux as the GZK cut-off. It is possible, in principle, that the suppression is due to the absence of astronomical sources capable to accelerate particles to the energies higher than $\sim 10^{20}$ eV. To identify the flux suppression with the GZK effect on the cosmic ray spectrum, one would need to detect the sources of UHECR and measure their individual spectra. If the high-energy flux suppression is due to the GZK effect, one would find that the UHECR flux from sources at the distances beyond 10-100 Mpc get gradually suppressed with the increasing distance to the source.

Detection of the sources of UHECR is difficult because of the low statistics of the signal. In fact, the errorbars at the highest energies in Fig. 2.27 are statistical: one just runs out os statistics above $10^{20}$ eV. Reading from the "y" axis of the figure, we see that the UHECR flux is $\simeq 10^{-11}/(\text{km}^2 \text{ s sr})$. To detect a single UHECR of the energy $10^{20}$ eV, one needs an exposure time of one year ($3 \times 10^7$ s) for the collection area of 3000 km.

This is the collection area of existing UHECR experiments, like Pierre Auger Observatory and Telescope Array. These experiments detect cosmic rays using a "hybrid" detection technique of extensive air showers, as shown in Fig. 2.25. Charged particles of the shower reaching the ground are detected by a network of detectors on the ground (on occasion, in Fig. 2.25 the detectors are scintillator pads). Fluorescence emission of nitrogen molecules excited along the path of the shower is detected by the air fluorescence telescopes monitoring the volume of the atmosphere above the surface particle detectors.

## 2.13.4 Pion and pair production in proton-proton collisions

Similar pair and pion production effects take place also in proton-proton collisions. Kinematics of the reaction allows to calculate the threshold. For example, in the case of pion production reaction the threshold is

$$E_{p,thr} = m_p \left(1 + \frac{m_\pi^2 + 4m_\pi m_p}{2m_p}^2\right) \qquad (2.198)$$

this gives numerically

$$E_{kin} = E_{p,thr} - m_p \simeq 280 \text{ MeV} \tag{2.199}$$

The cross-section of this reaction is also determined by the strong interactions and is about the geometrical cross-section of the proton,

$$\sigma_{pp} \simeq 4 \times 10^{-26} \text{ cm....} 10^{-25} \text{ cm} \tag{2.200}$$

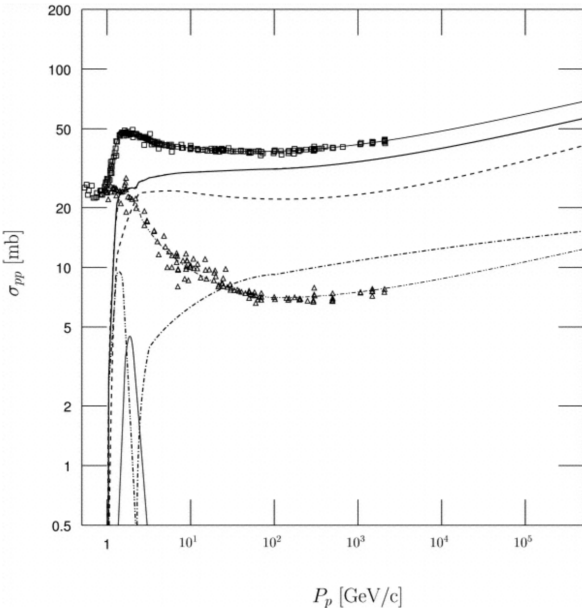depending on (growing with) the proton energy, see Fig. 2.28.



Figure 2.28:  Cross-section of proton-proton collisions.

As an example,we could consider propagation of cosmic ray protons in the interstellar medium.  Typical density of the interstellar medium around us is $n_{ISM} \sim 1 \text{ cm}^{-3}$. The mean free path of the proton is

$$\lambda_{pp} \simeq \frac{1}{\sigma_{pp} n_{ISM}} \simeq 3 - 10 \text{ Mpc} \tag{2.201}$$

Inelasticity of the reaction in the case of proton-proton collisions is quite high, $\kappa \simeq 0.5$, so that single collision takes away a sizeable fraction of the proton energy. The cooling time due to the pion production process is about $(1-3) \times 10^8$ yr. This is somewhat longer than the residence time of cosmic rays in the Galaxy, but still, a fraction of cosmic rays interacts in the Galactic Disk before escaping from it.

Neutral and charged pions $\pi^0, \pi^\pm$ are unstable particles which decay into $\gamma$-rays, $\pi^0 \to 2\gamma$, neutrinos and muons $\pi^\pm \to \mu^\pm + \nu_\mu$. Muons, in turn , are also unstable and decay into electrons and neutrinos $\mu^\pm \to e^\pm + \nu_e + \nu_\mu$. Thus, pion production in $pp$ collisions results in production of $\gamma$-rays, neutrinos and high-energy electron / positrons.

Gamma-ray emission induced by interactions of cosmic rays with the protons from the interstellar medium is the main source of high-energy $\gamma$-rays from the Milky Way galaxy, see Fig. 2.29.
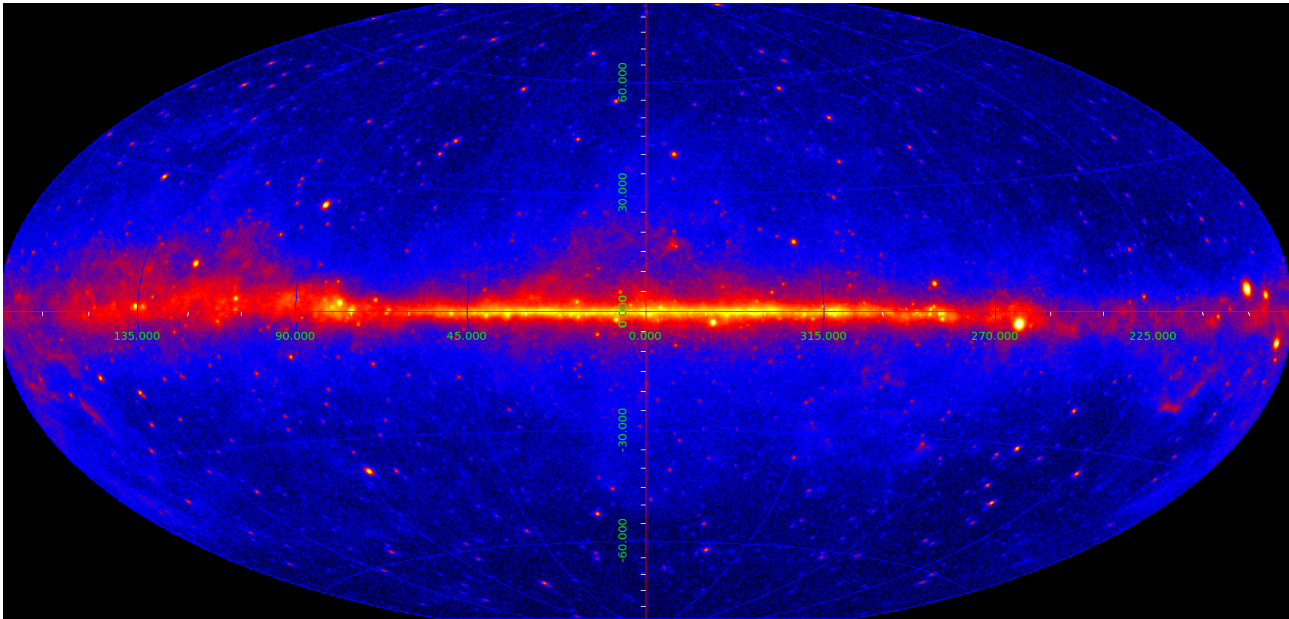
Figure 2.29: Fermi/LAT map of the sky in the energy range above 1 GeV. Diffuse emission from the Galactic Plane is dominated by the signal from interactions of cosmic ray protons with the interstellar medium with production of pions.

# Abbreviations

| | |
|---|---|
| AGN | Active Galactic Nucleus |
| FR I, FR II | Fanaroff-Riley radio galaxy, type I or type II |
| GRB | Gamma-Ray Burst |
| HMXRB | High-Mass X-ray Binary |
| LMXRB | Low-Mass X-ray Binary |
| PSR | Pulsar (name in astronomical catalogues) |
| PWN | Pulsar Wind Nebula |
| QSO | Quasi-Stellar Object (name in astronomical catalogues) |
| SNR | Supernova Remnant |
| Sy I, Sy II | Seyfert galaxy, type I or II |
| XRB | X-Ray Binary |

# Bibliography

[1] T.Courvoisier, *High-Energy Astrophysics*, Springer 2013.

[2] M.Longair, *High-Energy Astrophysics*, Third Edition, Cambridge Univ. Press, 2011.

[3] F.Aharonian, *Very High Energy Cosmic Gamma Radiation*, World Scientific, 2004.

[4] J. Beringer et al. (Particle Data Group), Phys. Rev. D86, 010001 (2012).

[5] T.Courvoisier, A&AR, 9, 1 (1998).

[6] J.Jackson, *Classical Electrondynamics*, Wiley & Sons, 1962.

[7] L.D.Landau, E.M.Lifshitz, *The Classical Theory of Fields*, Pergamon Press, 1971.

[8] Abdo A.A. et al., Ap.J., 696, 1084, 2009.

[9] Aharonian F. et al., Science, 314, 1424, 2006.

[10] Kreykenbohm I., et al., A&A, 433, L45, 2005.

[11] Hester J.J. ARA&A, 46, 127, 2008.

[12] Tavani M. et al., Science, 331, 736, 2011.

[13] Berezinsky V., Nucl.Phys.Proc.Suppl.188, 227 (2009) [arXiv:0901.0254]

[14] Ackermann M., et al., Ap.J., 750, 3 (2012).

[15] Ackermann M., et al., Science, 334, 1103 (2011).

[16] Berger E., ARA&A, 51, 43 (2014).

[17] S.Lee, Phys.Rev. D58, 043004 (1998).

[18] K.A. Olive et al. (Particle Data Group), Chin. Phys. C, 38, 090001 (2014)

[19] Yakovelv & Petchik, ARA&A, 42, 169 (2004)